



Search for PeV Gamma-Ray Emission from the Southern Hemisphere with 5 Yr of Data from the IceCube Observatory

M. G. Aartsen¹, M. Ackermann², J. Adams¹, J. A. Aguilar³, M. Ahlers⁴, M. Ahrens⁵, C. Alispach⁶, K. Andeen⁷, T. Anderson⁸, I. Ansseau³, G. Anton⁹, C. Argüelles¹⁰, J. Auffenberg¹¹, S. Axani¹⁰, P. Backes¹¹, H. Bagherpour¹, X. Bai¹², A. Balagopal V.¹³, A. Barbano⁶, S. W. Barwick¹⁴, B. Bastian², V. Baum¹⁵, S. Baur³, R. Bay¹⁶, J. J. Beatty^{17,18}, K.-H. Becker¹⁹, J. Becker Tjus²⁰, S. BenZvi²¹, D. Berley²², E. Bernardini^{2,56}, D. Z. Besson^{23,57}, G. Binder^{16,24}, D. Bindig¹⁹, E. Blaufuss²², S. Blot², C. Bohm⁵, M. Börner²⁵, S. Böser¹⁵, O. Botner²⁶, J. Böttcher¹¹, E. Bourbeau⁴, J. Bourbeau²⁷, F. Bradascio², J. Braun²⁷, S. Bron⁶, J. Brostean-Kaiser², A. Burgman²⁶, J. Buscher¹¹, R. S. Busse²⁸, T. Carver⁶, C. Chen²⁹, E. Cheung²², D. Chirkin²⁷, S. Choi³⁰, K. Clark³¹, L. Classen²⁸, A. Coleman³², G. H. Collin¹⁰, J. M. Conrad¹⁰, P. Coppin³³, P. Correa³³, D. F. Cowen^{8,34}, R. Cross²¹, P. Dave²⁹, C. De Clercq³³, J. J. DeLaunay⁸, H. Dembinski³², K. Deoskar⁵, S. De Ridder³⁵, P. Desiati²⁷, K. D. de Vries³³, G. de Wasseige³³, M. de With³⁶, T. DeYoung³⁷, A. Diaz¹⁰, J. C. Díaz-Vélez²⁷, H. Djumovic³⁸, M. Dunkman⁸, E. Dvorak¹², B. Eberhardt²⁷, T. Ehrhardt¹⁵, P. Eller⁸, R. Engel¹³, P. A. Evenson³², S. Fahey²⁷, A. R. Fazely³⁸, J. Felde²², K. Filimonov¹⁶, C. Finley⁵, A. Franckowiak², E. Friedman²², A. Fritz¹⁵, T. K. Gaisser³², J. Gallagher³⁹, E. Ganster¹¹, S. Garrappa², L. Gerhardt²⁴, K. Ghorbani²⁷, T. Glauch⁴⁰, T. Glüsenkamp⁹, A. Goldschmidt²⁴, J. G. Gonzalez³², D. Grant³⁷, Z. Griffith²⁷, S. Griswold²¹, M. Günder¹¹, M. Gündüz²⁰, C. Haack¹¹, A. Hallgren²⁶, L. Halve¹¹, F. Halzen²⁷, K. Hanson²⁷, A. Haungs¹³, D. Hebecker³⁶, D. Heereman³, P. Heix¹¹, K. Helbing¹⁹, R. Hellauer²², F. Henningsen⁴⁰, S. Hickford¹⁹, J. Hignight⁴¹, G. C. Hill⁴², K. D. Hoffman²², R. Hoffmann¹⁹, T. Hoinka²⁵, B. Hokanson-Fasig²⁷, K. Hoshina^{27,58}, F. Huang⁸, M. Huber⁴⁰, T. Huber^{2,13}, K. Hultqvist⁵, M. Hünnefeld²⁵, R. Hussain²⁷, S. In³⁰, N. Iovine³, A. Ishihara⁴³, G. S. Japaridze⁴⁴, M. Jeong³⁰, K. Jero²⁷, B. J. P. Jones⁴⁵, F. Jonske¹¹, R. Joppe¹¹, D. Kang¹³, W. Kang³⁰, A. Kappes²⁸, D. Kappesser¹⁵, T. Karg², M. Karl⁴⁰, A. Karle²⁷, U. Katz⁹, M. Kauer²⁷, J. L. Kelley²⁷, A. Kheirandish²⁷, J. Kim³⁰, T. Kintscher⁴⁶, J. Kiryluk⁴⁶, T. Kittler⁹, S. R. Klein^{16,24}, R. Koirala³², H. Kolanoski³⁶, L. Köpke¹⁵, C. Kopper³⁷, S. Kopper⁴⁷, D. J. Koskinen⁴, M. Kowalski^{2,36}, K. Krings⁴⁰, G. Krückl¹⁵, N. Kulacz⁴¹, N. Kurahashi⁴⁸, A. Kyriacou⁴², M. Labare³⁵, J. L. Lanfranchi¹, M. J. Larson²², F. Lauber¹⁹, J. P. Lazar²⁷, K. Leonard²⁷, A. Leszczyńska¹³, M. Leuermann¹¹, Q. R. Liu²⁷, E. Lohfink¹⁵, C. J. Lozano Mariscal²⁸, L. Lu⁴³, F. Lucarelli⁶, J. Lünemann³³, W. Luszczak²⁷, Y. Lyu^{16,24}, W. Y. Ma², J. Madsen⁴⁹, G. Maggi³³, K. B. M. Mahn³⁷, Y. Makino⁴³, P. Mallik¹¹, K. Mallot²⁷, S. Mancina²⁷, I. C. Mariş³, R. Maruyama⁵⁰, K. Mase⁴³, R. Maunu²², F. McNally⁵¹, K. Meagher²⁷, M. Medici⁴, A. Medina¹⁸, M. Meier²⁵, S. Meighen-Berger⁴⁰, T. Menne²⁵, G. Merino²⁷, T. Meures³, J. Micallef³⁷, D. Mockler³, G. Momenté¹⁵, T. Montaruli⁶, R. W. Moore⁴¹, R. Morse²⁷, M. Moulai¹⁰, P. Muth¹¹, R. Nagai⁴³, U. Naumann¹⁹, G. Neer³⁷, H. Niederhausen⁴⁰, S. C. Nowicki³⁷, D. R. Nygren²⁴, A. Obertacke Pollmann¹⁹, M. Oehler¹³, A. Olivas²², A. O'Murchadha³, E. O'Sullivan⁵, T. Palczewski^{16,24}, H. Pandya^{32,55}, D. V. Pankova⁸, N. Park²⁷, P. Peiffer¹⁵, C. Pérez de los Heros²⁶, S. Philippen¹¹, D. Pieloth²⁵, E. Pinat³, A. Pizzuto²⁷, M. Plum⁷, A. Porcelli³⁵, P. B. Price¹⁶, G. T. Przybylski², C. Raab³, A. Raissi¹, M. Rameez⁴, L. Rauch², K. Rawlins⁵², I. C. Rea⁴⁰, R. Reimann¹¹, B. Relethford⁴⁸, M. Renschler¹³, G. Renzi³, E. Resconi⁴⁰, W. Rhode²⁵, M. Richman⁴⁸, S. Robertson²⁴, M. Rongen¹¹, C. Rott³⁰, T. Ruhe²⁵, D. Ryckbosch³⁵, D. Rysewyk³⁷, I. Safa²⁷, S. E. Sanchez Herrera³⁷, A. Sandrock²⁵, J. Sandroos¹⁵, M. Santander⁴⁷, S. Sarkar⁵³, S. Sarkar⁴¹, K. Satalecka², M. Schaufel¹¹, H. Schieler¹³, P. Schlunder²⁵, T. Schmidt²², A. Schneider²⁷, J. Schneider⁹, F. G. Schröder^{13,32}, L. Schumacher¹¹, S. Sclafani⁴⁸, D. Seckel³², S. Seunarine⁴⁹, S. Shefali¹¹, M. Silva²⁷, R. Snihur²⁷, J. Soedingrekso²⁵, D. Soldin³², M. Song²², G. M. Spiczak⁴⁹, C. Spiering², J. Stachurska², M. Stamatikos¹⁸, T. Stanev³², R. Stein², P. Steinmüller¹³, J. Stettner¹¹, A. Steuer¹⁵, T. Stezelberger²⁴, R. G. Stokstad²⁴, A. Stöbl⁴³, N. L. Strotjohann², T. Stürwald¹¹, T. Stüttgen⁴, G. W. Sullivan²², I. Taboada²⁹, F. Tenholt²⁰, S. Ter-Antonyan³⁸, A. Terliuk², S. Tilav³², K. Tollefson³⁷, L. Tomankova²⁰, C. Tönnis³⁰, S. Toscano³, D. Tosi²⁷, A. Trettin², M. Tselengidou⁹, C. F. Tung²⁹, A. Turcati⁴⁰, R. Turcotte¹³, C. F. Turley⁸, B. Ty²⁷, E. Unger²⁶, M. A. Unland Elorrieta²⁸, M. Usner², J. Vandenbroucke²⁷, W. Van Driessche³⁵, D. van Eijk²⁷, N. van Eijndhoven³³, S. Vanheule³⁵, J. van Santen², M. Vraeghe³⁵, C. Walck⁵, A. Wallace⁴², M. Wallraff¹¹, N. Wandkowsky²⁷, T. B. Watson⁴⁵, C. Weaver⁴¹, A. Weindl¹³, M. J. Weiss⁸, J. Weldert¹⁵, C. Wendt²⁷, J. Werthebach²⁷, B. J. Whelan⁴², N. Whitehorn⁵⁴, K. Wiebe¹⁵, C. H. Wiebusch¹¹, L. Wille²⁷, D. R. Williams⁴⁷, L. Wills⁴⁸, M. Wolf⁴⁰, J. Wood²⁷, T. R. Wood⁴¹, K. Woschnagg¹⁶, G. Wrede⁹, D. L. Xu²⁷, X. W. Xu³⁸, Y. Xu⁴⁶, J. P. Yanez⁴¹, G. Yodh¹⁴, S. Yoshida⁴³, T. Yuan²⁷, and M. Zöcklein¹¹

IceCube Collaboration

¹ Dept. of Physics and Astronomy, University of Canterbury, Private Bag 4800, Christchurch, New Zealand

² DESY, D-15738 Zeuthen, Germany

³ Université Libre de Bruxelles, Science Faculty CP230, B-1050 Brussels, Belgium

⁴ Niels Bohr Institute, University of Copenhagen, DK-2100 Copenhagen, Denmark

⁵ Oskar Klein Centre and Dept. of Physics, Stockholm University, SE-10691 Stockholm, Sweden

⁶ Département de physique nucléaire et corpusculaire, Université de Genève, CH-1211 Genève, Switzerland

⁷ Dept. of Physics, Marquette University, Milwaukee, WI 53201, USA

⁸ Dept. of Physics, Pennsylvania State University, University Park, PA 16802, USA

⁹ Erlangen Centre for Astroparticle Physics, Friedrich-Alexander-Universität Erlangen-Nürnberg, D-91058 Erlangen, Germany

¹⁰ Dept. of Physics, Massachusetts Institute of Technology, Cambridge, MA 02139, USA

¹¹ III. Physikalisches Institut, RWTH Aachen University, D-52056 Aachen, Germany

¹² Physics Department, South Dakota School of Mines and Technology, Rapid City, SD 57701, USA

- ¹³ Karlsruhe Institute of Technology, Institut für Kernphysik, D-76021 Karlsruhe, Germany
¹⁴ Dept. of Physics and Astronomy, University of California, Irvine, CA 92697, USA
¹⁵ Institute of Physics, University of Mainz, Staudinger Weg 7, D-55099 Mainz, Germany
¹⁶ Dept. of Physics, University of California, Berkeley, CA 94720, USA
¹⁷ Dept. of Astronomy, Ohio State University, Columbus, OH 43210, USA
¹⁸ Dept. of Physics and Center for Cosmology and Astro-Particle Physics, Ohio State University, Columbus, OH 43210, USA
¹⁹ Dept. of Physics, University of Wuppertal, D-42119 Wuppertal, Germany
²⁰ Fakultät für Physik & Astronomie, Ruhr-Universität Bochum, D-44780 Bochum, Germany
²¹ Dept. of Physics and Astronomy, University of Rochester, Rochester, NY 14627, USA
²² Dept. of Physics, University of Maryland, College Park, MD 20742, USA
²³ Dept. of Physics and Astronomy, University of Kansas, Lawrence, KS 66045, USA
²⁴ Lawrence Berkeley National Laboratory, Berkeley, CA 94720, USA
²⁵ Dept. of Physics, TU Dortmund University, D-44221 Dortmund, Germany
²⁶ Dept. of Physics and Astronomy, Uppsala University, Box 516, S-75120 Uppsala, Sweden
²⁷ Dept. of Physics and Wisconsin IceCube Particle Astrophysics Center, University of Wisconsin, Madison, WI 53706, USA; analysis@icecube.wisc.edu
²⁸ Institut für Kernphysik, Westfälische Wilhelms-Universität Münster, D-48149 Münster, Germany
²⁹ School of Physics and Center for Relativistic Astrophysics, Georgia Institute of Technology, Atlanta, GA 30332, USA
³⁰ Dept. of Physics, Sungkyunkwan University, Suwon 16419, Republic of Korea
³¹ SNOLAB, 1039 Regional Road 24, Creighton Mine 9, Lively, ON, P3Y 1N2, Canada
³² Bartol Research Institute and Dept. of Physics and Astronomy, University of Delaware, Newark, DE 19716, USA
³³ Vrije Universiteit Brussel (VUB), Dienst ELEM, B-1050 Brussels, Belgium
³⁴ Dept. of Astronomy and Astrophysics, Pennsylvania State University, University Park, PA 16802, USA
³⁵ Dept. of Physics and Astronomy, University of Gent, B-9000 Gent, Belgium
³⁶ Institut für Physik, Humboldt-Universität zu Berlin, D-12489 Berlin, Germany
³⁷ Dept. of Physics and Astronomy, Michigan State University, East Lansing, MI 48824, USA
³⁸ Dept. of Physics, Southern University, Baton Rouge, LA 70813, USA
³⁹ Dept. of Astronomy, University of Wisconsin, Madison, WI 53706, USA
⁴⁰ Physik-department, Technische Universität München, D-85748 Garching, Germany
⁴¹ Dept. of Physics, University of Alberta, Edmonton, AB, T6G 2E1, Canada
⁴² Department of Physics, University of Adelaide, Adelaide, 5005, Australia
⁴³ Dept. of Physics and Institute for Global Prominent Research, Chiba University, Chiba 263-8522, Japan
⁴⁴ CTSPS, Clark-Atlanta University, Atlanta, GA 30314, USA
⁴⁵ Dept. of Physics, University of Texas at Arlington, 502 Yates St., Science Hall Rm. 108, Box 19059, Arlington, TX 76019, USA
⁴⁶ Dept. of Physics and Astronomy, Stony Brook University, Stony Brook, NY 11794-3800, USA
⁴⁷ Dept. of Physics and Astronomy, University of Alabama, Tuscaloosa, AL 35487, USA
⁴⁸ Dept. of Physics, Drexel University, 3141 Chestnut St., Philadelphia, PA 19104, USA
⁴⁹ Dept. of Physics, University of Wisconsin, River Falls, WI 54022, USA
⁵⁰ Dept. of Physics, Yale University, New Haven, CT 06520, USA
⁵¹ Department of Physics, Mercer University, Macon, GA 31207-0001, USA
⁵² Dept. of Physics and Astronomy, University of Alaska Anchorage, 3211 Providence Dr., Anchorage, AK 99508, USA
⁵³ Dept. of Physics, University of Oxford, Parks Road, Oxford OX1 3PU, UK
⁵⁴ Department of Physics and Astronomy, UCLA, Los Angeles, CA 90095, USA

Received 2019 September 5; revised 2020 January 16; accepted 2020 January 16; published 2020 February 27

Abstract

The measurement of diffuse PeV gamma-ray emission from the Galactic plane would provide information about the energy spectrum and propagation of Galactic cosmic rays, and the detection of a pointlike source of PeV gamma-rays would be strong evidence for a Galactic source capable of accelerating cosmic rays up to at least a few PeV. This paper presents several unbinned maximum-likelihood searches for PeV gamma-rays in the Southern Hemisphere using 5 yr of data from the IceTop air shower surface detector and the in-ice array of the IceCube Observatory. The combination of both detectors takes advantage of the low muon content and deep shower maximum of gamma-ray air showers and provides excellent sensitivity to gamma-rays between ~ 0.6 and 100 PeV. Our measurements of pointlike and diffuse Galactic emission of PeV gamma-rays are consistent with the background, so we constrain the angle-integrated diffuse gamma-ray flux from the Galactic plane at 2 PeV to $2.61 \times 10^{-19} \text{ cm}^{-2} \text{ s}^{-1} \text{ TeV}^{-1}$ at 90% confidence, assuming an E^{-3} spectrum, and we estimate 90% upper limits on pointlike emission at 2 PeV between 10^{-21} and $10^{-20} \text{ cm}^{-2} \text{ s}^{-1} \text{ TeV}^{-1}$ for an E^{-2} spectrum, depending on decl. Furthermore, we exclude unbroken power-law emission up to 2 PeV for several TeV gamma-ray sources observed by the High Energy Spectroscopic System and calculate upper limits on the energy cutoffs of these sources at 90% confidence. We also find no PeV gamma-rays correlated with neutrinos from IceCube's high-energy starting event sample. These are currently the strongest constraints on PeV gamma-ray emission.

Unified Astronomy Thesaurus concepts: Particle astrophysics (96); Galactic cosmic rays (567); Gamma-rays (637); Cosmic rays (329)

⁵⁵ Now at: Astrophysical Institute, Vrije Universiteit Brussel (VUB), B-1050 Brussels, Belgium.

⁵⁶ Also at Università di Padova, I-35131 Padova, Italy.

⁵⁷ Also at National Research Nuclear University, Moscow Engineering Physics Institute (MEPhI), Moscow 115409, Russia.

⁵⁸ Earthquake Research Institute, University of Tokyo, Bunkyo, Tokyo 113-0032, Japan.

1. Introduction

Cosmic rays arriving at Earth approximately follow a power-law energy spectrum over 11 orders of magnitude, from 1 GeV to 100 EeV, with a slightly changing spectral index and only a few notable features. The softening of the spectrum at the

“knee” at around 3 PeV and hardening of the spectrum at the “ankle” at around 3 EeV are the most prominent features of the spectrum. It is generally believed that the Galactic contribution to the cosmic-ray flux begins decreasing at the knee but extends up to the ankle, where the extragalactic population is responsible for the spectral hardening (Gaisser 2006). However, this belief remains unsubstantiated, since Galactic sources capable of accelerating cosmic rays above a PeV have not been identified yet. Cosmic-ray interactions with the gas near the accelerator produce neutrinos and gamma-ray photons. Unlike cosmic rays, neutrinos and gamma-rays are unaffected by magnetic fields and thus critical for the identification of these accelerators. Further, the cosmic rays that escape the local environment of their sources propagate through the Galaxy and interact with interstellar gas. The observable emission of neutrinos and gamma-rays is expected to peak along the Galactic plane, where most of the interstellar gas is concentrated (Kalberla & Kerp 2009). The measurement of this diffuse emission can provide information about the cosmic-ray diffusion processes and gauge the cosmic-ray spectrum at Galactic locations other than the Earth (Gaggero et al. 2015a; Acero et al. 2016).

The IceCube Observatory has observed an isotropic flux of astrophysical neutrinos (Aartsen et al. 2013c, 2014, 2015b), but no pointlike sources have been resolved so far, except for recent strong indications of an extragalactic source based on multimessenger observations (Aartsen et al. 2018). A recent study using neutrino data from both IceCube and ANTARES constrained the Galactic plane contribution to the isotropic flux to no more than 8.5% (Albert et al. 2018).

A complementary PeV gamma-ray search in the energy range of ~ 0.6 –100 PeV is made possible by the presence of the surface air shower component of the IceCube Observatory. In this energy regime, gamma-rays can only be observed over Galactic distances due to the high cross section for pair production with the cosmic microwave background radiation field (Protheroe & Biermann 1996). Therefore, the measurement of PeV gamma-rays can further constrain the Galactic contribution to the observed astrophysical neutrino flux. As the sole experiment to date that is sensitive to PeV gamma-rays in the Southern Hemisphere, the IceCube Observatory offers a unique window into high-energy processes in our Galaxy.

This paper will summarize the PeV gamma-ray measurements of the IceCube Observatory and is a follow-up to the previous study by Aartsen et al. (2013a), who used data taken over 1 yr with a partial configuration of IceCube consisting of 40 strings (IC-40). Here we analyze 5 yr of data from the completed observatory with 86 strings and include inclined events recorded only by the surface array, which significantly increases the detector acceptance over the entire field of view (FOV) of $-90^\circ \leq \delta \leq -53^\circ$ (decl.).

In the first part of this analysis, we obtain an air shower event sample rich in gamma-ray candidates by exploiting the key differences between air showers of cosmic-ray and gamma-ray origin. The most effective discriminator is the number of muons produced in the air shower. Muons are created in gamma-ray air showers from muon pair production, as well as the decay of photoproduced pions and kaons (Drees et al. 1989; Halzen et al. 2009). However, these processes are much less frequent than muon production from nucleus–nucleus interactions in hadronic showers. From CORSIKA (Heck et al. 1998) simulations utilizing the hadronic interaction models

FLUKA (Battistoni et al. 2007) and SYBILL 2.1 (Ahn et al. 2009), we find that 1 PeV vertical proton showers contain roughly

10 times the number of 1 GeV muons at the IceTop surface compared to 1 PeV vertical gamma-ray showers. This ratio increases to roughly 100 for muons with energy greater than 460 GeV at the surface. The in-ice array of IceCube is sensitive to muons that are highly collimated around the shower axis with energies greater than ~ 460 GeV at the surface. While the surface array is crucial to measure the energy deposited in the electromagnetic part of the shower, it is also sensitive to lower-energy muons arriving far from the shower core. Additionally, the shower maximum from gamma-ray primaries occurs, on average, deeper in the atmosphere, resulting in a younger shower age (Risse & Homola 2007). The stage of longitudinal shower development can be assessed from the electromagnetic component observed by the surface array. The gamma–hadron discrimination method is detailed in Section 3.3.

In the second part of this analysis, we search for pointlike sources of PeV gamma-rays in the Southern Hemisphere using the event sample containing gamma-ray-like events. The current generation of ground-based air Cerenkov detectors has uncovered a wealth of Galactic TeV gamma-ray sources (e.g., Carrigan et al. 2013; Abeysekara et al. 2017; Benbow et al. 2017). Of particular interest in this analysis are the results of the High Energy Spectroscopic System (H.E.S.S.), which has an FOV that overlaps with that of IceTop. H.E.S.S. is the only experiment to detect sources that show no evidence of a cutoff at TeV energies in a location testable by this analysis. These sources include pulsar wind nebulae (PWNs), supernova remnants (SNRs), and several other unclassified sources (Carrigan et al. 2013). We search for emission spatially correlated with these known TeV gamma-ray sources in addition to an unbiased search for PeV gamma-ray sources across the entire analysis FOV. We also search for PeV counterparts to the IceCube neutrino events with a high likelihood of astrophysical origin (Aartsen et al. 2015c), a component of which may be of Galactic origin (Ahlers & Murase 2014; Joshi et al. 2014; Kachelriess & Ostapchenko 2014; Ahlers et al. 2016). The search methods are described in Section 4.1 and the results of the point-source searches are presented in Sections 5.1–5.3.

Diffuse gamma-ray emission from the Galactic plane has been measured by ground-based air/water Cerenkov observatories up to ~ 10 TeV (Hunter et al. 1997; Aharonian et al. 2006; Abdo et al. 2008; Ackermann et al. 2012). In the Northern Hemisphere, CASA-MIA (Borione et al. 1998) has placed upper limits on a diffuse flux from the Galactic plane between 140 TeV and 1.3 PeV, while KASCADE-Grande has reported limits on an isotropic diffuse flux of gamma-rays from 100 TeV to 1 EeV (Apel et al. 2017). The IC-40 analysis (Aartsen et al. 2013a) produced the sole limit on the PeV flux from a section of the Galactic plane visible in the Southern Hemisphere. In the third part of this analysis, we search for a diffuse flux from the Galactic plane within the FOV of IceTop ($\delta \leq -53^\circ$). We use the neutral pion decay component of the Fermi-LAT diffuse emission model (Ackermann et al. 2012) as a spatial template in a maximum-likelihood analysis described in Section 4.2. The results of this search are presented in Section 5.4.

2. The IceCube Observatory

Located at the geographic South Pole, the IceCube observatory (sketched in Figure 1) consists of two major

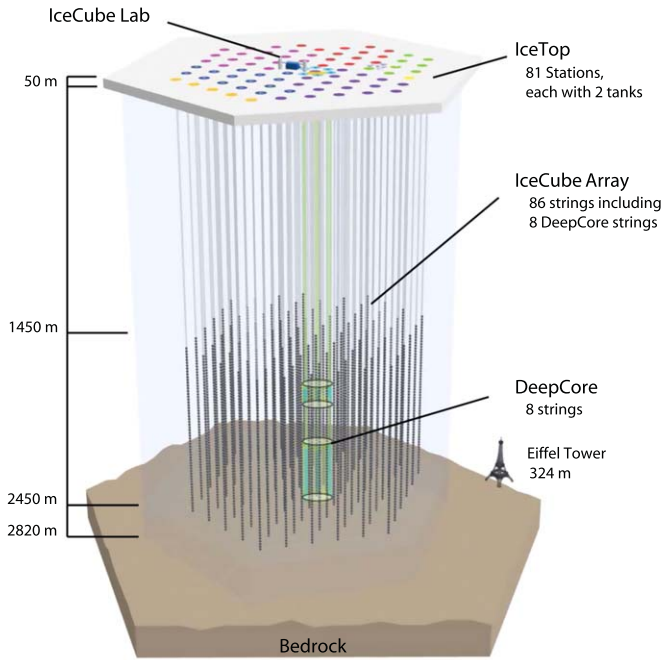


Figure 1. Schematic of the entire IceCube observatory (Aartsen et al. 2017b). The surface array (IceTop) and the in-ice array are shown, along with the in-ice subarray DeepCore.

components: an in-ice array and a companion surface array known as IceTop. The in-ice array is capable of detecting neutrinos in the energy range of 100 GeV to EeV and high-energy muons originating in cosmic-ray showers, whereas the surface array is designed to detect air showers from cosmic rays in the energy range of 300 TeV to EeV. The IceCube observatory (Aartsen et al. 2017b) was completed in 2010 following 7 yr of construction.

The cubic kilometer in-ice array is comprised of a total of 5160 optical sensors, or digital optical modules (DOMs), organized on 86 cables installed in the ice between depths of 1450 and 2450 m. Each DOM contains a 10 inch Hamamatsu photomultiplier tube (PMT), in addition to electronic boards necessary for triggering, digitization, and readout (Abbasi et al. 2009). The in-ice array detects the Cerenkov photons emitted by relativistic charged particles traversing the array.

The surface array of the IceCube observatory, IceTop (Abbasi et al. 2013), is located on top of the ice sheet at an altitude of 2835 m above sea level. The geometry of IceTop is displayed in Figure 2. IceTop is comprised of 81 stations, where a station is defined as two tanks filled with ice that are situated above a subset of IceCube strings. Each tank contains two DOMs embedded in ice and configured with different PMT gains in order to increase the dynamic range of signal measurement. In this way, each tank is capable of detecting the Cerenkov radiation from muons and other charged particles traversing it. IceTop triggers on extensive air showers by measuring the Cerenkov light inside the tanks emitted by air shower particles or secondary particles from their interactions in ice. At the surface, a typical cosmic-ray muon has an energy of a few GeV. Such minimum ionizing muons, passing through a tank, will deposit roughly the same amount of energy depending on their path length inside the tank. Every DOM’s charge spectrum from single muons, obtained from low-energy cosmic-ray showers, is fitted to find the charge value corresponding to vertical muons. Thus, all IceTop DOMs are calibrated

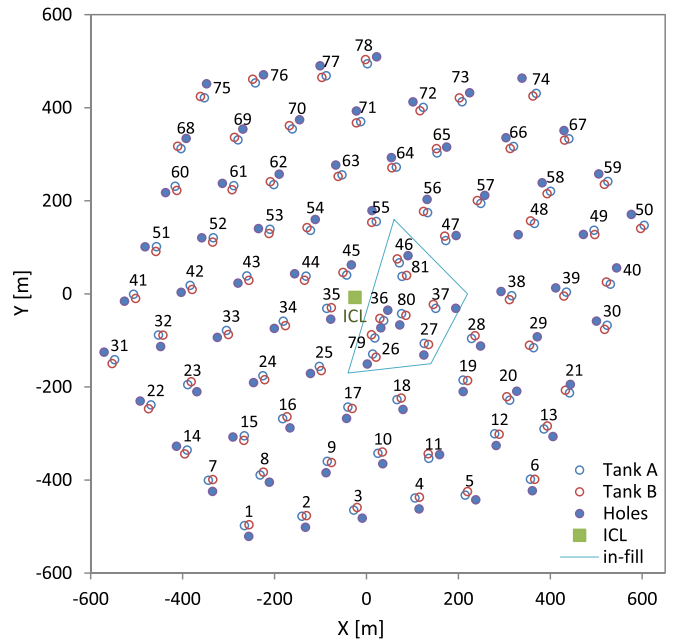


Figure 2. IceTop array geometry with locations for 81 stations and in-ice string holes. The stations that form the denser infill array for lower-energy showers are also demarcated.

to convert their charge value to a standard vertical equivalent muon (VEM) unit.

In this analysis, both the surface and in-ice arrays are used to discriminate gamma-ray-induced air showers from cosmic-ray-induced air showers. Reconstructions using IceTop signals for an air shower provide the energy proxy, arrival direction, and a primary mass-sensitive parameter (see Section 3.3.2), while the in-ice array provides an estimate of the energy deposited by \sim TeV muons for air showers whose axis passes through the deep ice detector.

3. Data Set Construction

Five years of experimental data are used in this analysis, collected between 2011 May and 2016 May. We use a machine-learning classifier to separate gamma-ray signal from the cosmic-ray background. During the training of this classifier, 10% of the observed data are used to model the background, leaving 90% available for the final analysis. Since the expected fraction of gamma-rays in the air shower data is very low ($\mathcal{O}(10^{-4})$), we use data in lieu of Monte Carlo simulations as a proxy for the cosmic-ray background. This greatly reduces the systematic dependencies inherent to simulation, such as the choice of hadronic interaction model, atmospheric model, cosmic-ray composition model, and snow height averaging. The total live time of the data used for each year in the final analysis is listed in Table 1. To model signal, Monte Carlo simulations of gamma-ray air showers were produced using CORSIKA version 7.37, with high-energy hadronic interactions treated with SYBILL 2.1 and low-energy hadronic interactions modeled using FLUKA. Of the gamma-ray Monte Carlo, 80% was used in the training of the event classifiers, with the remaining 20% withheld to test the final analysis performance. The simulated gamma-ray showers were weighted to a power-law spectrum, with the choice of spectral index depending upon the source hypothesis. Simulations and

Table 1
Data Sample Information

Data Year	Live Time (days)	λ_s (m)	N_{events} (total)	N_{events} (PS)	N_{events} (GP)
2011	308.7	2.10	27,551,210	97,034	68,286
2012	295.9	2.25	35,662,684	85,079	64,823
2013	321.4	2.25	35,215,316	107,009	79,787
2014	325.7	2.30	33,174,803	96,682	73,473
2015	325.2	2.30	30,244,777	85,657	61,907

Note. For each data year, the table shows the live time of the data runs used in the final analysis, the snow absorption length used in the charge correction, and the number of events before classification, classified as gamma-ray candidates by the point-source (PS) event selection, and classified as gamma-ray candidates by the galactic plane (GP) event selection.

data were treated identically with regard to event processing, selection, and reconstruction.

3.1. Air Shower Event Reconstruction

An event is recorded in IceTop whenever at least three stations (six tanks) are hit by a shower front within a time interval of $6 \mu\text{s}$. Then the data recorded from the collection of tanks for each event are filtered to remove uncorrelated background particle hits. The simultaneous reconstruction of shower size and arrival direction is carried out through the maximization of likelihood functions describing the lateral distribution of the signal and the shower front shape (Abbasi et al. 2013). The signal charge distribution, S , around the shower core in the shower frame of reference is known as the lateral distribution function (LDF). The LDF chosen to describe air shower events in IceTop is an empirically derived double logarithmic parabola. At a lateral distance R from the shower axis, the charge expectation S in an IceTop tank is defined as

$$S(R) = S_{125} \left(\frac{R}{125 \text{ m}} \right)^{-\beta - \kappa \log_{10}(R/125 \text{ m})}, \quad (1)$$

where S_{125} , also referred to as shower size, is the fitted signal strength at a reference distance of 125 m; β is the fitted slope parameter correlated with shower age; and $\kappa = 0.303$ is a constant determined through simulation studies. The shower size, S_{125} , is proportional to the energy of the primary particle and converted to a reconstructed energy, E_{reco} , using parameterization obtained from cosmic-ray simulations (Rawlins & Feusels 2015).

Accumulation of snow on top of the IceTop tanks suppresses the electromagnetic portion of the air shower, requiring a correction factor to the signal expectation defined as

$$S_i^{\text{corr}} = S_i \exp \left(\frac{h_s^i}{\lambda_s \cos \theta} \right), \quad (2)$$

where S_i^{corr} is the corrected signal expectation, h_s^i is the snow height above the tank i , θ is the reconstructed zenith angle of the shower, and λ_s is the effective absorption length in snow. The value for λ_s used for each analysis year is also listed in Table 1. The effective absorption length was optimized by comparing each year's snow-corrected S_{125} spectrum with the spectrum from the first year of operation with the least amount of snow. Snow on top of IceTop tanks is constantly increasing

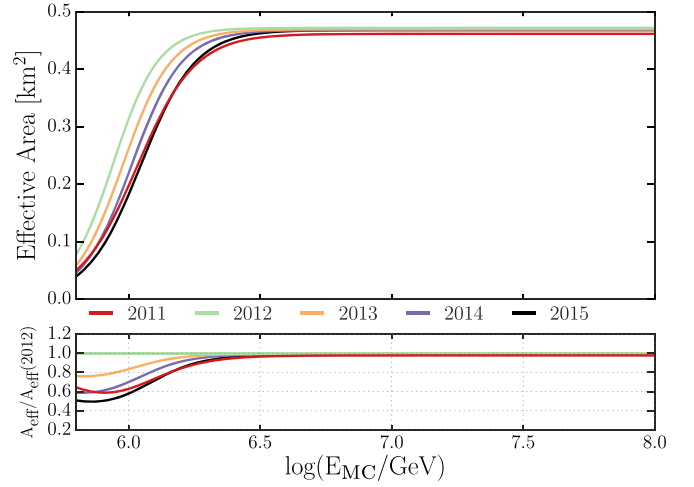


Figure 3. Effective area of IceTop to gamma-rays simulated with snow heights from each year of the data-taking period of the analysis. All cuts listed in Section 3 were applied.

at a rate of $\sim 20 \text{ cm yr}^{-1}$, which significantly degrades the detector acceptance. In order to accurately account for this effect, the detector response was simulated for each year of data included in the analysis using the same set of CORSIKA gamma-ray showers. For each data set, the snow level on top of the tanks was set to the snow heights measured during the austral summer season. Figure 3 shows the effective area of IceTop to gamma-rays for each year as a function of the primary energy, illustrating the event rate loss caused by increasing amounts of snow. The effective area is lower for the 2011 data year due to low statistics for events with less than eight stations because only one in three such events were being transmitted north from the South Pole in 2011.

3.2. Quality Event Selection

To ensure good energy and direction reconstruction, the following quality cuts were applied.

1. Events must trigger at least five IceTop stations (i.e., where both tanks in the station have DOMs with deposited charge within $1 \mu\text{s}$).
2. The energy and directional reconstructions must converge.
3. The reconstructed core position must be contained within the surface array geometry. Specifically, the event must satisfy $D/d > 1$, where D and d are defined in Figure 4.
4. The tank with the largest deposited charge must not lie on the edge of the IceTop array.
5. At least one IceTop tank must have a signal greater than six VEMs.
6. The reconstructed zenith angles satisfy $\cos(\theta) > 0.8$.
7. The reconstructed shower sizes satisfy $\log_{10}(S_{125}) > -0.25$.

We limit the event selection to $E_{\text{reco}} \leq 100 \text{ PeV}$, as extending to higher energies would have required additional higher-energy gamma-ray simulations for a negligible improvement in sensitivity.

Angular resolution, defined as the angular radius that contains 68% of reconstructed showers coming from a fixed direction, drives the sensitivity of searches for pointlike and extended sources. Figure 5 shows the angular resolution of

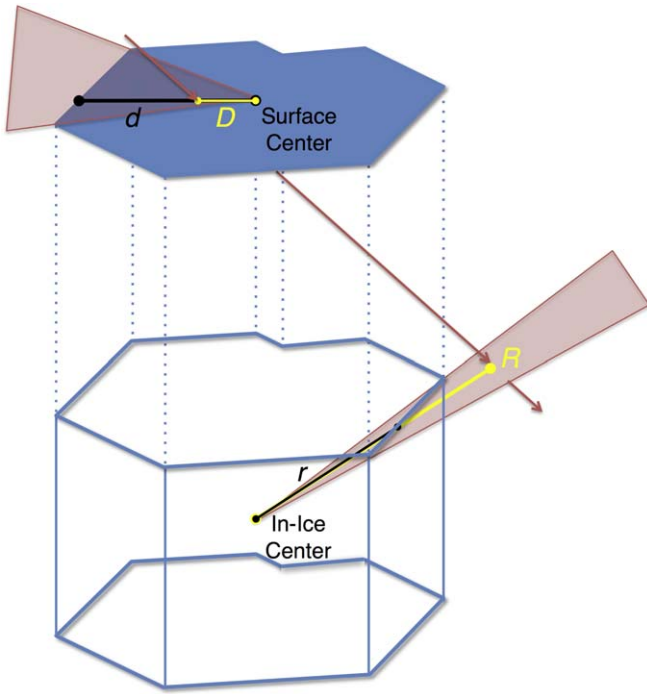


Figure 4. Schematic diagram representing the parameters used in the calculation of containment in IceTop and the in-ice array. For IceTop, D and d are the distances from the geometric center of the surface array to the shower core and the edge of the array in the direction of the shower core, respectively. For the in-ice array, R is the closest distance between the geometric center of the in-ice array and the reconstructed shower vertex, while r is the distance to the edge of the in-ice array along the same line.

simulated gamma-rays as a function of the true primary energy. The first and last years are shown to illustrate the impacts of the snow accumulation on the angular resolution, which amounts to a degradation of around 8%, on average.

3.3. Discriminating Gamma-Ray Showers

In order to extract all of the shower information correlated with the type of the primary particle, both surface and in-ice components of the detector are utilized. Section 3.3.1 details the technique used to obtain clean data from the in-ice array that informs on the number of high-energy muons in the shower. Section 3.3.2 describes the implementation of a new likelihood method that optimally retrieves information from the surface array correlated with the number of low-energy muons, shower age, and shower profile. IceTop-based shower discrimination allows us to include showers that do not pass through the in-ice array in the analysis. While the loss of in-ice information for these showers reduces the separation power, there is a large increase in detector acceptance at higher zenith angles, which is displayed in Figure 6. We combine the in-ice and surface components in a single classifier using machine learning as described in Section 3.3.3.

3.3.1. High-energy Muons in Ice

Muons that have energy greater than ~ 460 GeV at the surface are capable of generating light that can be detected by the photomultipliers of the in-ice array. This is the main parameter used to judge the hadronic content of air showers with trajectories that pass through the in-ice detector component. We use the total charge measured in-ice as a

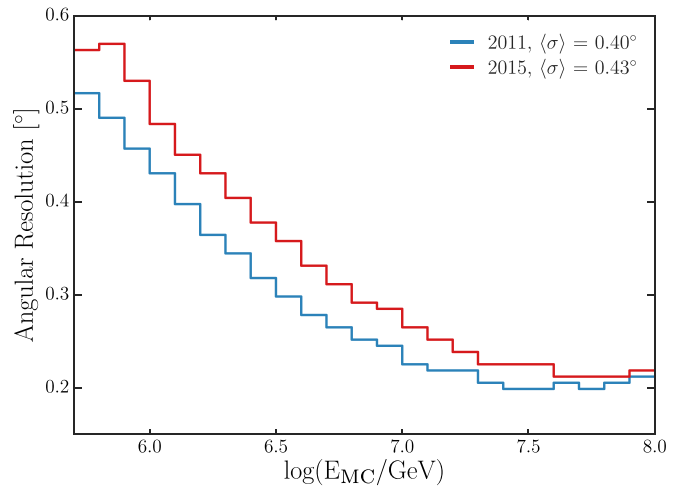


Figure 5. The 68% containment intervals of angular resolution to gamma-rays from a simulation using a detector response with snow heights from the first and last year of the data-taking period of the analysis. Here $\langle\sigma\rangle$ denotes the median angular resolution assuming an $E^{-2.0}$ energy spectrum.

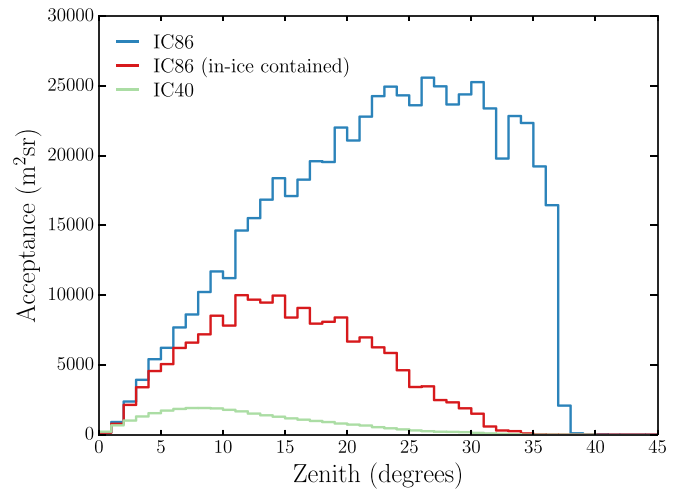


Figure 6. Detector acceptance (effective area integrated over solid angle) as a function of the zenith angle for all gamma-rays (blue line), the subset of gamma-rays passing through the in-ice array (red line), and the IC-40 analysis (green line; Aartsen et al. 2013a). The detector response for the IC-86 gamma-ray simulations shown here was done using snow heights from 2012 October. All three distributions were made assuming an $E^{-2.7}$ gamma-ray spectrum.

discriminating feature. In order to isolate the signal produced by muons, a cleaning procedure is applied to remove charge deposited by uncorrelated background particles. The cleaning procedures for events with or without an in-ice trigger are described below.

Nearest or next-to-nearest neighboring DOMs on the same string that have deposited charge (a “hit”) within a time window of $\pm 1 \mu\text{s}$ are designated to be in hard local coincidence (HLC). An in-ice trigger is defined as eight or more such HLC hits in an event within a $5 \mu\text{s}$ time window. An in-ice trigger that falls between 3.5 and $11.5 \mu\text{s}$ after the start of an IceTop trigger is considered coincident, in which case, hits outside of the coincident time window are removed. Next, HLC hits are used as seeds in a hit selection algorithm that searches for single hits that are within 150 m and $1 \mu\text{s}$ of each seed

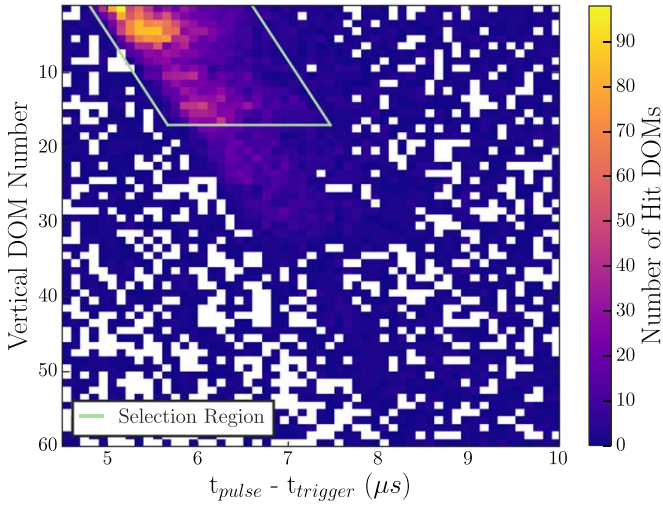


Figure 7. Number of in-ice array hit DOMs binned in vertical DOM number and the hit time (t_{hit}) relative to the IceTop trigger (t_{trigger}) for a collection of experimental events that have no in-ice array HLC hits. The vertical DOM number denotes the position of the hit DOM on its string; larger numbers are on deeper layers of the array. The green box delimits the region within which charge is selected for event classification.

DOM. In an iterative manner, single hits that satisfy the criteria are included in the seeds, and the search is performed again. This is repeated three times. The combined charge of the final selection of hits is used as a discriminating feature.

For those events that have only an IceTop trigger, simpler cleaning is applied. For HLC hits, a time window selection is used to reduce the uncorrelated muon background, optimized to be between 3.5 and 9 μs after the trigger in IceTop. Hadronic showers may produce isolated hits in IceCube without an HLC flag. This is illustrated in Figure 7, which displays the number of single hits as a function of vertical DOM number (analogous to depth) and time with respect to the trigger for a collection of events that have no HLC hits. There is a clear excess of hits near the top of the detector that is suitable for classification. A selection window is optimized by a maximization of the ratio of signal and square root noise. We define the front of the time window for charge selection as

$$t_{\text{start}} = \frac{4.8\mu\text{s} + d_{\text{DOM}}/c}{\cos(\theta)}, \quad (3)$$

where θ is the reconstructed zenith angle of the event, d_{DOM} is the depth of the hit in meters, and c is the speed of light. Hits are retained if they fulfill the following criteria, represented by the green box shown in Figure 7.

1. The hit is within 130 m of the reconstructed shower axis.
2. The hit is within the top 16 layers of in-ice DOMs.
3. The hit has a time stamp t , such that $t_{\text{start}} < t < t_{\text{start}} + 1.8\mu\text{s}$.

3.3.2. IceTop Shower Footprint

As discussed in Section 2, minimum ionizing muons passing through an IceTop tank deposit charge such that the peak of the muon charge distribution is at ~ 1 VEM with a width attributed to the zenith angle distribution of muons (Abbasi et al. 2013). At a sufficiently large distance from the shower core, the electromagnetic component becomes subdominant, and the

characteristic ~ 1 VEM signals from GeV muons can be discerned. Figure 8 shows a probability distribution function (PDF) describing the distribution of the charges as a function of the lateral distance from the reconstructed shower core, also called the LDF, for simulated gamma-rays and observed cosmic rays. The prominent muon signal can be seen emerging in the cosmic-ray PDF beyond ~ 200 m, while it is very diminished in the gamma-ray PDF. The local charge fluctuations, observed as the width of the charge distribution for a given lateral distance in Figure 8, are also a measure of the hadronic content of the shower. The longitudinal development stage of the shower is reflected in the slope of the LDF seen in Figure 8. The curvature of the shower front, i.e., the arrival time distribution of particles as a function of the lateral distance, is also sensitive to the longitudinal stage of the shower as it reaches the IceTop surface.

We construct three two-dimensional PDFs that incorporate these shower front properties. For this, we use information from individual IceTop tanks, which are indexed from $1 \leq i \leq 162$. The PDFs are constructed using tank charges $\{Q_i\}$, their lateral distances from the reconstructed shower axis $\{R_i\}$, and hit times with respect to the expected planar shower front arrival time $\{\Delta T_i\}$. Gamma-ray simulations and 10% of cosmic-ray data are used to construct the PDFs for the gamma-ray $\{H_\gamma\}$ and cosmic-ray $\{H_{\text{CR}}\}$ hypotheses, respectively. Unhit and inactive tanks are included in the PDFs by assigning artificial and fixed values to charge and time ($Q_i = 0.001$ VEM and $\Delta T_i = 0.01$ ns) outside the range of hit tank values. The lateral distance distribution of unhit tanks (as seen in the bottom of the plots in Figure 8) also contributes to the differences between the gamma-ray and cosmic-ray PDFs.

Based on each of the three two-dimensional PDFs, a log-likelihood ratio is calculated for all events. For instance, the log-likelihood ratio using the lateral charge distribution for a given event is defined as

$$\Lambda_{\text{QR}} = \log_{10} \left(\frac{L_{\text{QR}}(\text{event}|H_\gamma)}{L_{\text{QR}}(\text{event}|H_{\text{CR}})} \right), \quad (4)$$

where the likelihood L_{QR} is defined as

$$L_{\text{QR}}(\text{event}|H) = \prod_{i=1}^{162} P(Q_i, R_i | H), \quad (5)$$

with $P(Q_i, R_i | H)$ being the probability of observing a tank with measured charge Q_i and at lateral distance R_i for the hypothesis H . Hit tanks for a sample cosmic-ray event, overlaid on the PDFs in Figure 8 using open squares, illustrate how such an event would collect a greater likelihood from the cosmic-ray PDF as compared to the gamma-ray PDF.

Similarly, one can calculate $\Lambda_{Q\Delta T}$ and $\Lambda_{\Delta TR}$ from the PDFs that describe the time distribution of charges and the shower front curvature. The sum of all three log-likelihood ratios is then used as an input to a random forest classifier described in Section 3.3.3. The hadronic content and the longitudinal development stage of the shower at the surface depend on the primary energy and zenith angle, in addition to the mass of the primary particle. To reduce this dependence, the construction of PDFs and calculation of the log-likelihood ratio is carried out in $\log_{10}(S_{125})$ bins of 0.1 and $\cos(\theta)$ bins of 0.05.

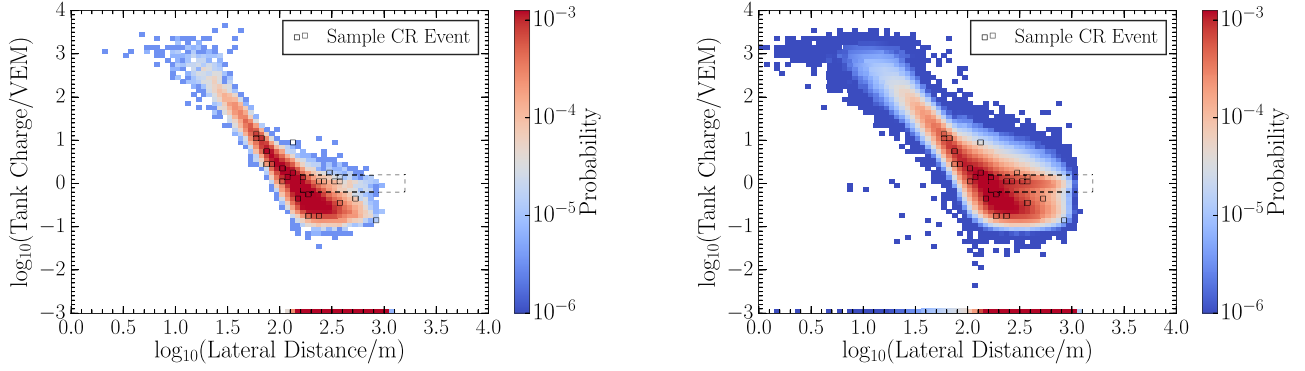


Figure 8. IceTop PDFs, describing the charge distribution as a function of the lateral distance of the tank from the shower axis, for simulated gamma-ray (left) and observed cosmic-ray (right) events with $0.3 \leq \log_{10}(S_{125}) < 0.4$ and $0.95 \leq \cos(\theta) < 1.0$. Hit tanks for one sample cosmic-ray event are indicated by open squares in both PDFs, and the feature attributed to GeV muons is highlighted using dashed lines.

3.3.3. Random Forest

The final event selection is performed using a random forest classifier implemented using the open-source Python software Scikit-learn (Pedregosa et al. 2011). In total, five features are included in the training process.

1. The total charge deposited in the in-ice array after applying the cleaning procedure described in Section 3.3.1.
2. The likelihood sum as described in Section 3.3.2.
3. The energy proxy $\log_{10}(S_{125})$.
4. The cosine of the reconstructed zenith angle.
5. A parameter that describes the containment of the shower axis within the in-ice array, defined to be $C = R/r$, where R and r are defined in Figure 4.

To prevent overtraining, the maximum tree depth is limited to 8. The output of the random forest is a score between zero and 1, with 1 being the most gamma-ray-like. The signal threshold for classifying events as gamma-rays is chosen to be 0.7. These values were optimized through a cross-validation grid search on sensitivity performance. Tuning the additional hyperparameters of the random forest showed negligible impact, and they were kept at their default values.

Due to the differences in flux expectation, the gamma-ray spectrum used for training the classifier is different for the point source and diffuse cases. For point sources, in order to be robust in performance to a range of spectral indices, we use two classifiers: one trained with a relatively hard ($E^{-2.0}$) spectrum and the other with a relatively soft ($E^{-2.7}$) spectrum. In this case, the event is retained if either classifier returns a score above the signal threshold value. For the diffuse case, a single random forest trained with an $E^{-3.0}$ spectrum is used (see Section 5.4 for the motivation behind the choice of spectral index). Figure 9 illustrates the fraction of events that pass the signal threshold cut as function of energy. The total number of events classified as gamma-rays under these criteria for both cases are listed in Table 1 for each analysis year.

4. Likelihood Analysis Methods

All source hypotheses considered in this analysis were tested through an unbinned likelihood ratio method following the prescription of Braun et al. (2008). The form of the likelihood is dependent on the source class considered.

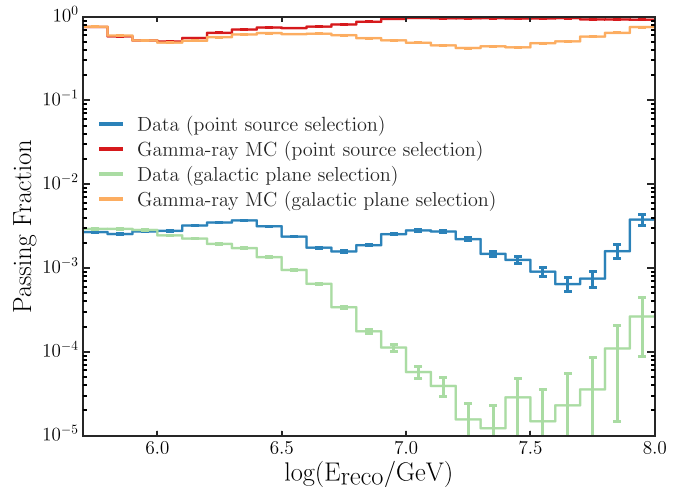


Figure 9. Fraction of events that pass the gamma-hadron discrimination cut for gamma-ray simulation and data (cosmic-ray background) as a function of energy. Both the point-source and Galactic plane component event selections are shown.

4.1. Point Sources

Sources that are pointlike or extended in TeV gamma-ray astronomy should appear pointlike in this analysis. Hence, we construct a point-source hypothesis for an unbiased source search in our entire FOV, as well as for targeted H.E.S.S. source searches. The likelihood under this assumption takes the form

$$L = \prod_j \prod_{i \in j} \left(\frac{n_s^j}{N^j} S_i^j(|\mathbf{x}_i - \mathbf{x}_s|, E_i, \sigma_i; \gamma) + \left(1 - \frac{n_s^j}{N^j} \right) B_i^j(\delta_i, E_i) \right). \quad (6)$$

The likelihood L is a product over i events in each of j data sets, where each data set is comprised of 1 yr of data. For a data set j , n_s^j is the number of signal events originating from the point source, and N^j is the total number of events. Each event has a direction $\mathbf{x}_i = (\alpha_i, \delta_i)$ consisting of an R.A. α_i and decl. δ_i , an energy E_i , and an angular uncertainty σ_i . The events are compared to a point-source hypothesis comprised of a direction

\mathbf{x}_S and spectral index γ . For the single source case, the signal PDF S_i^j is defined as

$$S_i^j = \frac{1}{2\pi\sigma_i^2} e^{-\frac{|\mathbf{x}_i - \mathbf{x}_S|^2}{2\sigma_i^2}} \mathcal{E}_{S,i}^j(E_i, \delta_i, \gamma), \quad (7)$$

where the angular uncertainty is included using a Gaussian distribution with σ_i . Here $\mathcal{E}_{S,i}^j$ is the normalized signal energy distribution. The background PDF is defined as

$$B_i^j = \frac{1}{2\pi} B_{\text{exp}}^j(\delta_i) \mathcal{E}_{B,i}^j(E_i, \delta_i), \quad (8)$$

where B_{exp}^j is the decl.-dependent detector acceptance to cosmic rays derived from data, and $\mathcal{E}_{B,i}^j$ is the normalized background energy distribution. The background PDF is uniform in R.A. and constructed from cosmic-ray data randomized in R.A.

The likelihood is maximized with respect to n_s and γ , where n_s is the total number of signal events proportionally distributed among the signal events n_s^j of each data set according to the effective area and live time of the samples. This yields the best-fit values \hat{n}_s and $\hat{\gamma}$ and a test statistic defined as

$$TS = -2 \log \left(\frac{L(n_s = 0)}{L(\hat{n}_s, \hat{\gamma})} \right). \quad (9)$$

To evaluate the significance of an observed test statistic, a background test statistic ensemble is constructed from scrambled data using random R.A. values for the event directions. The p -value is the fraction of the ensemble that has a test statistic exceeding the observed value. When relevant, the number of independent trials performed (e.g., the number of H.E.S.S. source locations tested individually) is accounted for, and a posttrial p -value is reported for the search.

To gauge the analysis sensitivity to point sources, a range of simulated fluxes is injected on top of the scrambled data events. The sensitivity is defined as the flux that produces a test statistic above the median of the background-only trial ensemble at the injected direction in 90% of the trials. This is equivalent to the Neyman 90% confidence level construction (Neyman 1941). The discovery potential is defined as the flux that achieves a 5 σ detection in 50% of the trials.

When searching for emission from the selected H.E.S.S. point sources, we include a test for signal from all sources combined. This stacking approach requires a modification to the likelihood, which we implement following the method in Aartsen et al. (2017a). For a catalog of M point-source locations, the signal PDF is constructed as

$$S_i^j = \frac{\sum_m^M R_m^j(\delta_m) e^{-\frac{|\mathbf{x}_i - \mathbf{x}_S|^2}{2\sigma_i^2}}}{\sum_m^M R_m^j(\delta_m)} \mathcal{E}_{S,i}^j(E_i, \delta_i, \gamma), \quad (10)$$

where R_m^j is the relative detector acceptance to gamma-rays at the location of the source m . In this form, the sources are weighted assuming equal flux at Earth for each source.

4.2. Diffuse Source

The source hypotheses for the Galactic plane and cascade neutrino (see Section 5.3) searches extend spatially over a significant portion of the sky. For these cases, it is no longer valid to treat the signal as having a negligible contribution to

the background PDF by averaging the R.A. Instead, a modification to the likelihood is made, following a method first introduced by Aartsen et al. (2015a) in a binned likelihood approach and later applied in an unbinned likelihood by Aartsen et al. (2017c), whose formulation we use here.

The background term B_i^j in Equation (6) is replaced with two terms, \tilde{D}_i^j and \tilde{S}_i^j , which are the event densities of the experimental data and gamma-ray simulation, respectively, after averaging over R.A.:

$$L = \prod_j \prod_{i \in j} \left(\frac{n_s^j}{N^j} S_i^j(\mathbf{x}_i, \sigma_i, E_i; \gamma) + \tilde{D}_i^j(\sin \delta_i, E_i) - \frac{n_s^j}{N^j} \tilde{S}_i^j(\sin \delta_i, E_i) \right). \quad (11)$$

The construction of the signal PDF S begins with a model of the gamma-ray flux distribution over the entire FOV. This raw signal term must be convolved with the detector response to produce the expected observed distribution of emission in direction and energy. This is executed through a bin-by-bin multiplication of the relative detector acceptance to gamma-rays, determined through simulation, and the flux model. The point-spread function of each event, described as a Gaussian distribution of width σ , is accounted for through the convolution of the signal map with a range of σ from 0°.1 to 1°.0 in steps of 0°.05. On an event-by-event basis, the map corresponding to the σ of the event is used as the signal PDF S .

5. Results

5.1. All-sky Point-source Search

An unbiased search for a point source is accomplished by scanning over the entire FOV. The position of a single point source is assumed to lie in the direction of a given pixel in a HEALPIX map ($N_{\text{side}} = 512$, pixel diameter of 0°.11; Gorski et al. 2005). A test statistic is calculated using Equation (6) under this hypothesis. This process is repeated for each pixel in the analysis FOV. The resulting p -values of this scan, before accounting for trials, are shown in Figure 13. The region of the sky with a zenith angle $>5^\circ$ is excluded, as within this region, scrambling in R.A. alone is insufficient to build independent background trials.

The hottest spot in the sky, with a pretrial p -value of 4×10^{-5} , is located at -73.4° in decl. and 148.4° in R.A., with $n_s = 67.9_{-16.6}^{+17.8}$ and a spectral index of $2.9_{-0.3}^{+0.3}$. The posttrial p -value, calculated by comparing the observed test statistic to the background ensemble of hottest-spot test statistic values, is 0.18, consistent with the background expectation. Figure 10 shows the sensitivity and discovery potential to point sources of this analysis as a function of decl. The proportion of showers which are contained in IceCube drops sharply at higher shower inclinations, resulting in a decrease in performance at high decl. values.

5.2. TeV Gamma-Ray Source Studies at PeV Energies

There are a total of 15 TeV gamma-ray sources in the FOV of this analysis that have no evidence of a cutoff in their energy spectrum; all of these sources were reported by the H.E.S.S. collaboration. Table 2 lists the name of each source paired with the citation that provided the H.E.S.S. fit information, along with the best-fit decl. and spectral index observed by H.E.S.S.

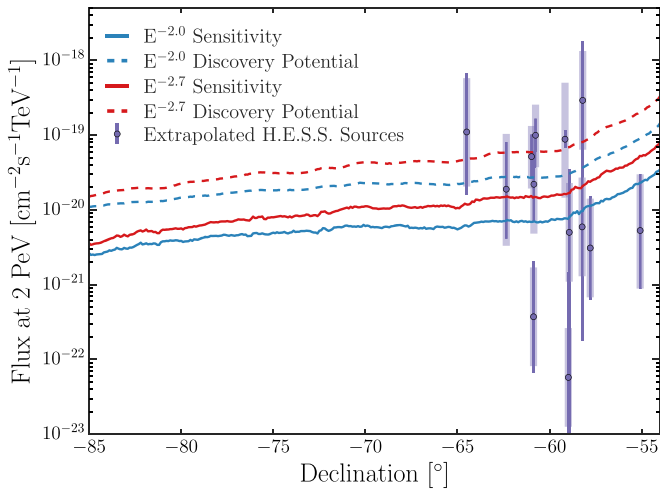


Figure 10. The sensitivity and discovery potential thresholds to a gamma-ray flux at Earth for $E^{-2.0}$ (solid) and $E^{-2.7}$ (dashed) point sources as a function of decl. are shown in blue and red, respectively. In purple are the extrapolated fluxes up to 2 PeV of H.E.S.S. sources in the analysis FOV, under the scenario of no break in the best-fit energy spectrum, with an approximate correction for absorption using model predictions from Lipari & Vernetto (2018). Error bars indicate the statistical uncertainty, while the systematic uncertainty is represented by the shaded areas.

The projected flux at 2 PeV of these sources, assuming there is no cutoff in their energy spectra, is shown in Figure 10. Attenuation effects were calculated for the Galactic coordinates and distance of each source using model results provided by Lipari & Vernetto (2018). Source distances were estimated from associated X-ray or radio observations when possible (Wakely & Horan 2008). Otherwise, a distance of 8.5 kpc, roughly that of the Galactic center, is assumed. The directions of the sources are shown overlaid on the all-sky scan in Figure 11.

In the first test of these sources, each source location is evaluated independently, making no assumption about the spectral index of the source. The pretrial p -value for every considered source resulting from this test is reported in Table 2. The most significant individual source, HESS J1427–608, has a pretrial p -value of 0.07, with a fitted n_s of $25.9^{+16.6}_{-15.7}$ and spectral index of $3.2^{+0.8}_{-0.7}$. This results in a trial-corrected p -value of 0.65, consistent with the background expectation.

To place constraints on the fluxes of these sources individually, we consider the case where the flux of each source extends with no cutoff in energy and with the spectral index observed by H.E.S.S. Under this flux assumption, we report the 90% confidence level upper limit on the flux at 2 PeV at Earth for each source in Table 2 as $\Phi_{90\%}$. We note that uncertainties in the best-fit H.E.S.S. spectrum have a negligible effect on the upper limits and their relationship to the extrapolated flux.

For a subset of the sources, our limits are strong enough to place constraints on an energy cutoff of the source flux. Here we assume the flux to be the combination of a power law and an exponential energy cutoff at E_{cut} :

$$\Phi(E) = \Phi_{\text{P.L.}}(E)e^{-E/E_{\text{cut}}}. \quad (12)$$

The value of E_{cut} was determined by evaluating, for a range of energy cutoff values, the resulting flux of the source and the analysis sensitivity for the same hypothesis. Here we do incorporate absorption from Lipari & Vernetto (2018) in order

to limit the energy cutoff at the source. The minimum energy cutoff value where our sensitivity lies below the flux expectation of the source is reported in Table 2 as a 90% confidence level upper limit on E_{cut} .

We additionally search for combined PeV emission from all of the H.E.S.S. sources. In this test, all of the sources are stacked using the modified signal PDF from Equation (10), which weights the sources assuming equal flux at Earth for each source. The result of this stacking correlation test is a p -value of 0.08, consistent with the background.

5.3. IceCube HESE Neutrino Correlation

From the 4 yr high-energy starting event (HESE) neutrino sample (Aartsen et al. 2015c), a total of 11 events lie within the FOV of this analysis. The event positions and 1σ uncertainties are overlaid on the pretrial p -value map of the all-sky point-source search in a polar projection in Figure 14. There are two topologically distinct event types, referred to as cascades and tracks. We treat the event types separately.

Cascade neutrino events are produced by neutral-current interactions, as well as charged-current interactions of electron and tau neutrinos. These events have poor angular resolution, typically greater than 10° in the HESE sample. In order to correctly account for the change in detector acceptance over such a large point-spread function, we test for a correlation with these cascade neutrino events using the template likelihood method described in Section 4.2. The signal template is constructed by combining the spatial likelihood contour PDFs for each event. The correlation test resulted in a conservative p -value of >0.5 . We place a 90% confidence level upper limit of $1.07 \times 10^{-19} \text{ cm}^{-2} \text{ s}^{-1} \text{ TeV}^{-1}$ on the flux at 2 PeV of a source class consistent with the HESE cascade directions and an $E^{-2.0}$ spectrum.

Track neutrino events are the product of charged-current muon neutrino interactions. These interactions produce muons that can travel several kilometers through the ice, which allows for reconstructions with an angular resolution of $<1.2^\circ$ for events in the HESE sample. There is one track event in our FOV, which we treat under the point-source prescription. At a decl. of $\delta = -86.77^\circ$, scrambling events in R.A. alone is insufficient to build a background test statistic distribution; instead, we scramble events randomly throughout the polar cap region of $>5^\circ$ zenith angle, within which acceptance was found to be approximately even. No evidence of signal was found in the test for a point source at the event location, which resulted in a conservative p -value of >0.5 .

5.4. Diffuse Galactic Plane Template Analysis

To test for a diffuse flux from the Galactic plane, the template likelihood method is employed, with the signal template taken to be the pion decay component of the Fermi-LAT diffuse emission model (Ackermann et al. 2012). The Fermi-LAT template multiplied by the detector acceptance is shown in Figure 15 for the 2012 sample.

The expected observed spectral index of diffuse gamma-rays from the Galactic plane is still an open question due to existing uncertainties in the Galactic cosmic-ray spectrum, interstellar gas distribution, and flux attenuation. The unattenuated flux at PeV energies has been predicted to be as hard as E^{-3} (Ingelman & Thunman 1996; Vernetto & Lipari 2017), although the

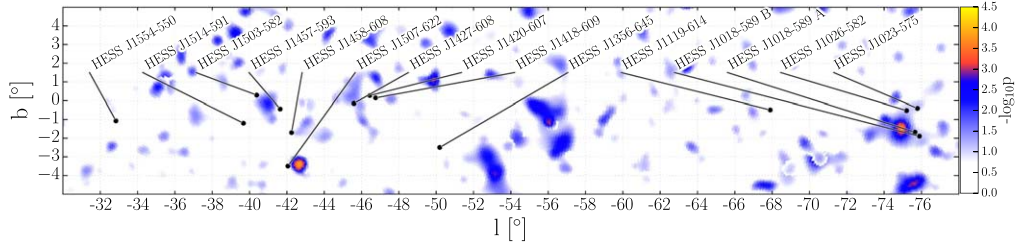


Figure 11. All-sky likelihood scan pretrial p -value shown in Galactic coordinates for $|b| > 5$. The H.E.S.S. sources in the analysis FOV are shown in black.

Table 2
H.E.S.S. Source Target Catalog

Source	Type	Decl. (deg)	Spectral Index	p -value	$\Phi_{90\%}$ (2 PeV) ($\text{cm}^{-2} \text{s}^{-1} \text{TeV}^{-1}$)	Distance (kpc)	E_{cut} U.L. (PeV)	Reference
HESS J1356–645	PWN	–64.50	2.20	>0.50	7.66×10^{-21}	2.4	0.9	1
HESS J1507–622	PWN	–62.35	2.24	0.29	1.42×10^{-20}	8.5 ^b	16.6	2
HESS J1119–614 ^a	Unidentified	–61.40	N/A	0.30	N/A	5.0	N/A	3, 13
HESS J1418–609	SNR	–60.98	2.22	0.31	1.34×10^{-20}	5.0	3.5	4
HESS J1458–608	Unidentified	–60.87	2.80	0.22	2.56×10^{-20}	8.5 ^b	—	5
HESS J1427–608	PWN	–60.85	2.20	0.07	1.96×10^{-20}	8.5 ^b	25.9	6
HESS J1420–607	PWN	–60.76	2.17	0.49	8.84×10^{-21}	5.6	1.4	4, 14
HESS J1457–593 ^a	SNR	–59.47	N/A	>0.50	N/A	8.5 ^b	N/A	7
HESS J1514–591	PWN	–59.16	2.27	0.52	1.02×10^{-20}	5.2	1.5	8, 15
HESS J1018–589 B	PWN	–58.98	2.90	0.08	4.12×10^{-20}	8.5 ^b	—	9
HESS J1018–589 A	Unidentified	–58.93	2.20	0.07	2.17×10^{-20}	8.5 ^b	—	9
HESS J1503–582	Unidentified	–58.23	2.40	0.17	2.77×10^{-20}	8.5 ^b	—	10
HESS J1026–582	PWN	–58.20	1.94	0.09	1.83×10^{-20}	2.3	1.4	11, 16
HESS J1023–575	Unidentified	–57.79	2.58	0.08	4.60×10^{-20}	8.0	—	11, 17
HESS J1554–550	PWN	–55.08	2.10	>0.50	2.29×10^{-20}	9.0	—	12, 18

Notes. Shown first are the source type, decl., and best-fit spectral index by H.E.S.S. for each candidate source. Next, we give the pretrial p -value observed by this analysis and 90% confidence level upper limits on the flux at 2 PeV at Earth assuming the H.E.S.S. best-fit spectral index and no cutoff in energy. Finally, we show the best-known distance to each source and a 90% confidence level upper limit on the energy cutoff of the source assuming an extrapolation of the H.E.S.S. best-fit power-law spectrum with an energy cutoff and absorption from Vernetto & Lipari (2017). Sources where this analysis cannot limit the energy cutoff are denoted by dashes.

^a Sources with no reported spectral index, in which case we do not report source specific limits.

^b Sources without an X-ray or radio observation are given a value of 8.5 kpc, approximately the distance to the Galactic center.

References. (1) Abramowski et al. (2011b), (2) Acero et al. (2011), (3) Djannati-Ataï et al. (2010), (4) Aharonian et al. (2006), (5) de los Reyes et al. (2012), (6) Aharonian et al. (2008), (7) Hofverberg et al. (2010), (8) Aharonian et al. (2005), (9) Abramowski et al. (2012), (10) Renaud et al. (2008), (11) Abramowski et al. (2011a), (12) Acero (2011), (13) Crawford et al. (2001), (14) Kishishita et al. (2012), (15) Gaensler et al. (1999), (16) Keith et al. (2008), (17) Rauw et al. (2011), (18) Sun et al. (1999).

spectrum could be as soft as $E^{-3.4}$ (Ingelman & Thunman 1996) after attenuation. Here we fix the spectral index to 3.

Maximization of the likelihood in Equation (11) returns an observed test statistic corresponding to a p -value of 0.28, which provides no evidence of a diffuse signal from the Galactic plane under the current hypothesis. We place a 90% confidence level upper limit of $2.61 \times 10^{-19} \text{ cm}^{-2} \text{ s}^{-1} \text{ TeV}^{-1}$ on the normalization of the spectral energy distribution at 2 PeV with spectral index 3. The normalization energy was chosen to be 2 PeV, as that is the energy for which the analysis was found to be least sensitive to the spectral index assumption.

As previous experimental limits have used a box region around the Galactic plane to describe the diffuse emission, for a limit comparison, we use an angular-integrated scaled flux,

$$\Phi_{\text{template}} = \Phi \Delta\Omega \frac{\int_{\text{all-sky}} S_{\text{Fermi}} d\Omega}{\int_{\Delta\Omega} S_{\text{Fermi}} d\Omega}, \quad (13)$$

where the angular-integrated flux from the observed region is $\Phi \Delta\Omega$, and the second term scales this flux by the fraction of the Galactic plane emission present in the observed region as given

by the Fermi-LAT pion decay template S_{Fermi} . This is, in effect, a limit on the overall normalization of the Fermi template flux. Figure 12 compares the scaled flux limits from this analysis with the existing IC-40 (Aartsen et al. 2013a) and CASH (Borione et al. 1998) limits, as well as the measured flux by ARGO-YBJ (Bartoli et al. 2015). In addition, the gamma-ray flux from the diffuse Galactic plane in the analysis FOV is shown for two model predictions from Lipari & Vernetto (2018). The first assumes that cosmic-ray spectra have a space-independent spectral shape throughout the Galaxy. The second assumes that the central part of the Galaxy has a harder cosmic-ray spectrum than observed at Earth, an idea supported by some recent analyses (Gaggero et al. 2015b; Yang et al. 2016).

5.5. Systematics

There are a number of systematic uncertainties that can affect the estimated sensitivity of the study, including the snow attenuation, the calibration of the charge deposited in IceTop tanks, the hadronic interaction and ice models used in simulations, and the anisotropy of the cosmic-ray flux. For

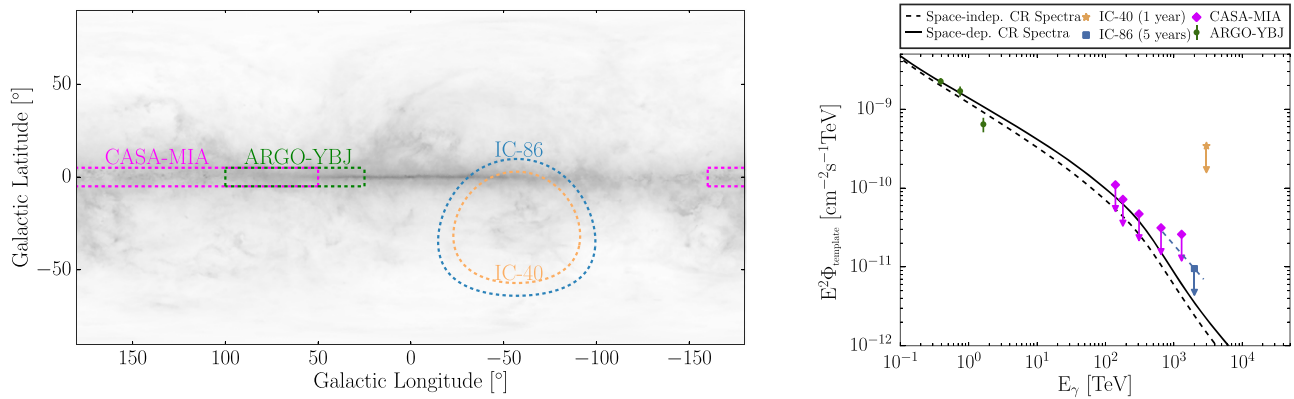


Figure 12. Left: respective FOVs of CASA-MIA (Borione et al. 1998), ARGO-YBJ (Bartoli et al. 2015), IC-40 (Aartsen et al. 2013a), and this analysis overlaid on a map of the π^0 decay component of the Fermi-LAT Galactic plane diffuse emission model (Ackermann et al. 2012). Right: IceCube 90% confidence level upper limit (IC-86) on the angular-integrated scaled flux from the Galactic plane in our FOV for a spatial distribution of emission given by the π^0 decay component of the Fermi-LAT diffuse emission model. The IC-86 upper limit is compared to results from ARGO-YBJ, CASA-MIA, and IC-40 using the scaling defined in Equation (13). Dotted lines show the E^{-3} spectrum, used for obtaining IceCube upper limits, over the energy range containing 5%–95% events in the final sample. Also shown for two models are the absorbed flux predictions for the IC-86 FOV calculated by Lipari & Vernetto (2018) by special request. The two models assume space-independent and space-dependent cosmic-ray spectra throughout the Galaxy, respectively.

each systematic component, data sets are constructed using the parameter uncertainty bounds. These data sets are propagated through the entire analysis chain to evaluate the corresponding uncertainty in sensitivity. Here we report both point-source and Galactic plane analysis sensitivity uncertainties. For the point-source sensitivity, we assume the median uncertainty based on a scan over the decl. range in 0.1° bins. These data sets were constructed from events not used in the training of the random forest classifier detailed in Section 3.3.3.

The optimal value for the snow attenuation coefficient λ , used in the charge correction for IceTop tanks as shown in Equation (2), has been found to vary by ± 0.2 m over a range of zenith angle and energy values (Aartsen et al. 2013b). A more thorough model of the snow attenuation is a work in progress; for this work, we quote this bound as a conservative estimate. This systematic results in an uncertainty of 11.0% in sensitivity to point sources and 11.2% in sensitivity to a diffuse flux from the Galactic plane.

The calibration of the IceTop tank charge to VEM units requires a fitting of the muon peak in the charge spectrum of the tank (Abbasi et al. 2013). The dependence of this fit to systematic factors was studied in detail by Van Overloop (2011). They found an uncertainty of at most $\pm 3\%$ on the charge calibration, which propagates directly to an uncertainty in the deposited signal. This systematic error results in an uncertainty of 2.1% in sensitivity to point sources and 7.4% in sensitivity to a diffuse flux from the Galactic plane.

The number of muons generated in simulated gamma-ray air showers at energies sufficient to trigger the detectors is governed by the high-energy hadronic interaction model used in CORSIKA. In order to evaluate the magnitude of the model dependence, we perform sensitivity studies with simulations generated using QGSJetII-04 (Ostapchenko 2011) but otherwise identical to the original set. We chose QGSJetII-04 over other post-Large Hadron Collider models because it was the model that produced the most muons in hadronic air showers (Plum et al. 2018). Sensitivities calculated with these systematic data sets resulted in a 23.2% uncertainty for point sources and a 26.2% uncertainty for a diffuse flux from the Galactic plane.

The anisotropy of the cosmic-ray flux is a potential source of signal contamination. While decl.-dependent anisotropy is accounted for due to the use of data to construct the

background PDF in the likelihood, any anisotropy in R.A. is not. However, within the analysis FOV, this anisotropy is at a level of at most 0.03% (Aartsen et al. 2016). This is negligible in relation to statistical uncertainties, which are $\sim 25\%$ in flux at the sensitivity threshold.

In simulation, the uncertainties in the optical properties of the ice can affect the amount of charge measured. While this has a potential for systematic error, an analysis with data sets using $\pm 10\%$ in deposited charge in IceCube showed negligible impact on sensitivity compared to statistical fluctuations. Finally, the method we use naturally corrects for any bias in the energy proxy. Any systematic biases in fitted n_s and γ values that are unaccounted for are found to be negligible when compared to statistical uncertainties.

Under the assumption that the errors discussed are independent and Gaussian-distributed, the overall sensitivity uncertainty resulting from quadrature addition is 25.8% for point sources and 29.4% for the Galactic plane.

6. Discussion and Conclusion

We have presented the results of multiple searches for PeV gamma-rays using 5 yr of data from 2011 to 2016 collected by the IceCube Observatory. For all flux hypotheses considered, no significant excess in emission above background expectation was observed.

An unbiased scan over the entire analysis FOV resulted in a decl.-dependent 90% confidence level upper limit of $\sim 10^{-21}$ – $10^{-20} \text{ cm}^{-2} \text{ s}^{-1} \text{ TeV}^{-1}$ on the flux at 2 PeV of a gamma-ray point source, the most stringent PeV gamma-ray point-source limits to date and an improvement of more than an order of magnitude over the previous IceCube analysis (Aartsen et al. 2013a).

In addition, we searched for PeV gamma-ray emission of H.E.S.S. sources that show no evidence for a spectral cutoff at TeV energies. For the first time, upper limits have been placed on the high-energy emission of these sources. For seven sources, these limits exclude the spectra observed by H.E.S.S. from extending without a cutoff to PeV energies after accounting for absorption. The lowest-energy cutoff limit value is 900 TeV for the source HESS J1356–645. Figure 16 illustrates the extrapolated flux for this source with a 900 TeV

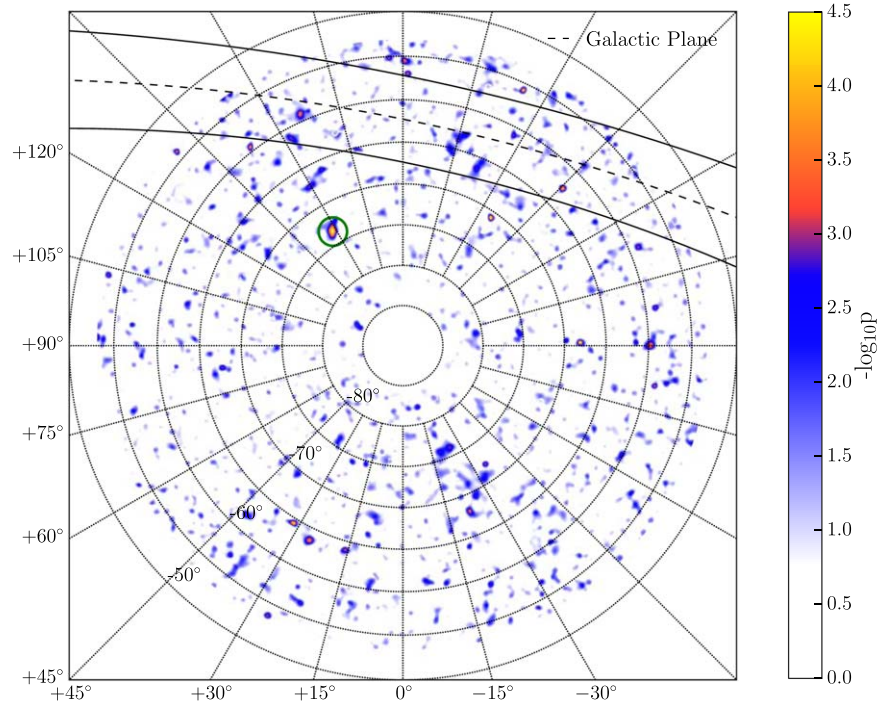


Figure 13. All-sky likelihood scan pretrial p -values shown projected from the South Pole in equatorial units. The R.A. is labeled along the figure axes, with the interior text denoting decl. bands. The green circle highlights the hottest spot in the scan. The Galactic plane region ($>5^\circ$ in Galactic latitude) is also shown.

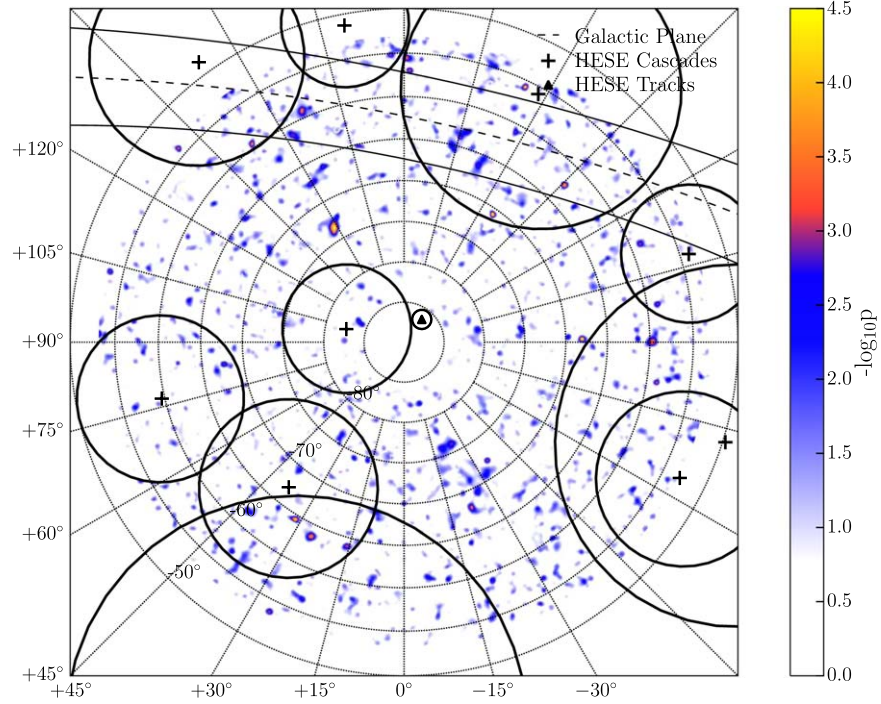


Figure 14. Reconstructed directions and 1σ uncertainties of events from the 4 yr HESE neutrino sample superimposed on the all-sky scan results.

cutoff in energy along with the corresponding 90% upper limits set by this analysis to the same flux assumptions. Considering the systematic/statistical uncertainties in the H.E.S.S. measurements, the measurement of the source distance, and those presented in Section 5.5, we do not expect sensitivity to spectral assumptions that slightly differ from our own. We present these constraints as order-of-magnitude estimates for

other spectral assumptions that may have, for example, additional spectral softening or a cutoff other than a simple exponential.

Since this analysis was executed, a new Galactic plane survey paper was published by the H.E.S.S. Collaboration that included a reanalysis of the sources included in this study (Abdalla et al. 2018). For all cases, the new analysis positions,

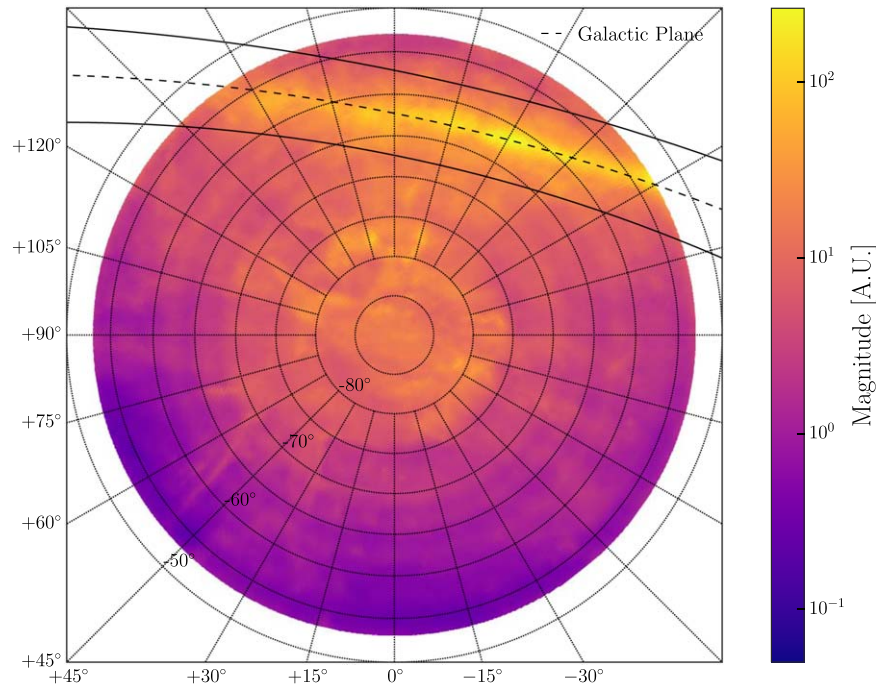


Figure 15. Fermi-LAT π^0 decay spatial template multiplied by the detector acceptance for the data year 2012.

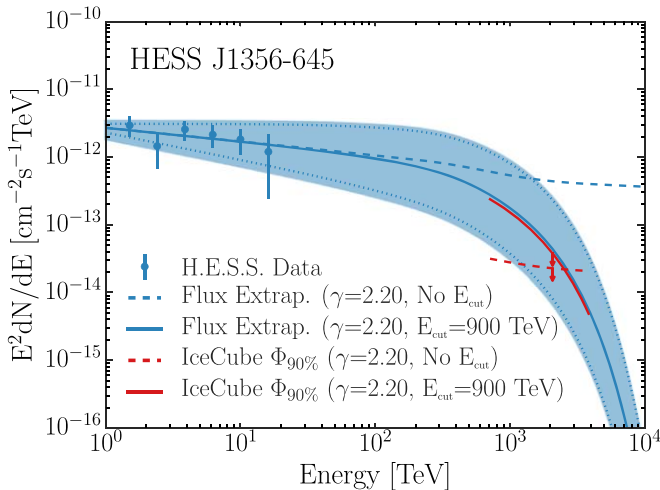


Figure 16. Flux measurements of the source HESS J1356-645 (Abramowski et al. 2011b), along with a power-law spectrum with (solid line) and without (dashed line) a 900 TeV cutoff in energy, where absorption is included for the source distance of 2.4 kpc (Wakely & Horan 2008) for both. For the cutoff extrapolation, the shaded region denotes the statistical uncertainty, while the systematic uncertainty is represented by dotted lines. The 90% confidence level upper limit to these flux extrapolations is shown in red.

spectral indices, and flux normalizations at 1 TeV are consistent with the values used for calculating the presented upper limits within statistical and systematic errors. The largest discrepancy in fit values is for the source HESS J1427-608, which had a best-fit spectral index of 2.20 in Aharonian et al. (2008). Guo et al. (2017) reported on a counterpart seen in Fermi-LAT data at GeV energies with a best fit including the H.E.S.S. data from Aharonian et al. (2008) of E^{-2} over four orders of magnitude in energy with no break in the spectrum, a property unique among currently known TeV sources. However, in Abdalla et al. (2018), the reanalysis best-fit spectral index was found to be 2.85.

The point-source map in the Galactic plane region shown in Figure 11 has several interesting spots with low p -values. The first is spatially coincident with the binary source HESS J1302-638 at $b = -0^\circ.99$ and $l = -55^\circ.81$ (Aharonian et al. 2005). This source was excluded from the targeted search, as TeV emission has only been observed during the periastron of the source, which occurs only once every 3.4 yr due to a highly eccentric orbit (Romoli et al. 2017). One such periastron occurred during the collection period of data used in this analysis in 2014. However, a follow-up analysis with only the data from the 2014 period showed no evidence for PeV gamma-ray emission from this direction. The second spot, near HESS J1507-622, is interesting because both the source and the spot lie on the edge of a large, nearby CO molecular cloud observed by Dame et al. (2001) that is most likely ~ 400 pc away. The type of the source has not been established, and it has a uniquely high Galactic latitude ($\sim 3^\circ.5$; Acero et al. 2011). This allows for the possibility of the source being nearby. However, the offset from the spot to the source location and the most dense region of the molecular cloud makes any association unlikely.

The correlation test between PeV gamma-ray candidate events and neutrino events from the IceCube HESE sample that lie within the FOV of this analysis also yields a null result.

We place a 90% confidence level upper limit of $2.61 \times 10^{-19} \text{ cm}^{-2} \text{ s}^{-1} \text{ TeV}^{-1}$ on the angular-integrated diffuse gamma-ray flux from the Galactic plane at 2 PeV under the assumption of an E^{-3} spectrum. Figure 12 (left) compares the FOVs of the different experiments. Here it is worth noting that the current analysis (IC-86) constrains PeV diffuse flux from a denser region of the Galactic plane than CASA-MIA (Borione et al. 1998). As shown in Figure 12 (right), the IC-86 upper limit is an order of magnitude better than the IC-40 result and the most stringent constraint on the diffuse flux above 1 PeV. The IC-86 upper limit is also compared to two model predictions for attenuated diffuse flux from the Galactic plane in the IceCube FOV as given by Lipari & Vernetto (2018).


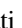

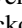





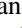
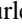

Both models derive diffuse gamma-ray emission under appropriate assumptions for the cosmic-ray flux throughout the Milky Way, interstellar gas distribution, and gamma-ray absorption effects. The model labeled “Space-dep. CR Spectra” includes a changing spectral index of the gamma-ray spectrum as a function of the distance to the Galactic center to reproduce the effects of a harder cosmic-ray spectrum near the Galactic center. The two model predictions are not too different for the IC-86 FOV, since it observes a part of the Galactic plane sufficiently far from the Galactic center. Even though the IC-86 upper limit cannot constrain the partially empirical model predictions by Lipari & Vernetto (2018), it may serve as important data for other detailed simulations of Galactic cosmic-ray transport, such as Gaggero et al. (2015b).

IceCube’s sensitivity to the gamma-ray flux is expected to improve at a rate lower than the inverse square root of the live time expected from additional exposure. This is due to the reduced acceptance to gamma-ray air showers with continued snow accumulation on IceTop tanks. A proposed scintillator array (Huber et al. 2017) at the surface will improve the sensitivity to the electromagnetic shower component and counteract the degradation of the photon sensitivity due to snow accumulation. Furthermore, radio antennas at the surface may improve the gamma–hadron separation and increase the sky coverage such that the Galactic center comes into the FOV (Balagopal et al. 2018). In the long term, a 7.9 km³ next-generation IceCube detector (van Santen et al. 2018) is being designed along with a 75 km² surface scintillator array. Adding radio antennas and nonimaging air Cerenkov telescopes to the surface array would provide sensitivity to PeV gamma-rays over a much larger FOV than the current detector. Recent hints of a PeVatron (Abramowski et al. 2016) near the Galactic center and the expected increase in the diffuse flux toward the Galactic center are strong motivators to search for PeV gamma-rays in the future with higher-sensitivity instruments. A future gamma-ray analysis with the IceCube observatory would be complementary to the planned experiments LHAASO (Cui et al. 2014) and HiSCORE (Tluczykont et al. 2014) in the Northern Hemisphere. Such an analysis would be aided in a search for galactic point sources by results from the proposed southern CTA site, which will provide even higher-energy measurements than H.E.S.S. of possible PeVatrons in the Southern Hemisphere (Acharya et al. 2013).

This work is in memory of Stefan Westerhoff. The IceCube collaboration acknowledges the significant contributions to this manuscript from Zachary Griffith and Hershail Pandya. We acknowledge support from the following agencies: USA—U.S. National Science Foundation Office of Polar Programs, U.S. National Science Foundation Physics Division, Wisconsin Alumni Research Foundation, Center for High Throughput Computing (CHTC) at the University of Wisconsin–Madison, Open Science Grid (OSG), Extreme Science and Engineering Discovery Environment (XSEDE), U.S. Department of Energy National Energy Research Scientific Computing Center, Particle Astrophysics Research Computing Center at the University of Maryland, Institute for Cyber-Enabled Research at Michigan State University, and Astroparticle Physics Computational Facility at Marquette University; Belgium—Funds for Scientific Research (FRS-FNRS and FWO), FWO Odysseus and Big Science programs, and Belgian Federal Science Policy Office (Belspo); Germany—Bundesministerium

für Bildung und Forschung (BMBF), Deutsche Forschungsgemeinschaft (DFG), Helmholtz Alliance for Astroparticle Physics (HAP), Initiative and Networking Fund of the Helmholtz Association, Deutsches Elektronen Synchrotron (DESY), and High Performance Computing Cluster of the RWTH Aachen; Sweden—Swedish Research Council, Swedish Polar Research Secretariat, Swedish National Infrastructure for Computing (SNIC), and Knut and Alice Wallenberg Foundation; Australia—Australian Research Council; Canada—Natural Sciences and Engineering Research Council of Canada, Calcul Québec, Compute Ontario, Canada Foundation for Innovation, WestGrid, and Compute Canada; Denmark—Villum Fonden, Danish National Research Foundation (DNRF), Carlsberg Foundation; New Zealand—Marsden Fund; Japan—Japan Society for Promotion of Science (JSPS) and Institute for Global Prominent Research (IGPR) of Chiba University; Korea—National Research Foundation of Korea (NRF); Switzerland—Swiss National Science Foundation (SNSF); United Kingdom—Department of Physics, University of Oxford.

ORCID iDs

M. Ahrens  <https://orcid.org/0000-0003-0709-5631>
 E. Bernardini  <https://orcid.org/0000-0003-3108-1141>
 P. Dave  <https://orcid.org/0000-0002-3879-5115>
 J. J. DeLaunay  <https://orcid.org/0000-0001-5229-1995>
 P. Desiati  <https://orcid.org/0000-0001-9768-1858>
 P. A. Evenson  <https://orcid.org/0000-0001-7929-810X>
 A. Franckowiak  <https://orcid.org/0000-0002-5605-2219>
 D. Kang  <https://orcid.org/0000-0002-5149-9767>
 U. Katz  <https://orcid.org/0000-0002-7063-4418>
 A. Kheirandish  <https://orcid.org/0000-0001-7074-0539>
 N. Park  <https://orcid.org/0000-0002-4282-736X>
 M. Santander  <https://orcid.org/0000-0001-7297-8217>
 S. Sarkar  <https://orcid.org/0000-0002-3542-858X>
 M. Song  <https://orcid.org/0000-0002-6167-2017>
 C. F. Turley  <https://orcid.org/0000-0002-9689-8075>
 J. Vandenbroucke  <https://orcid.org/0000-0002-9867-6548>
 D. L. Xu  <https://orcid.org/0000-0003-1639-8829>

References

- Aartsen, M. G., Abbasi, R., Abdou, Y., et al. 2013a, *PhRvD*, **87**, 062002
 Aartsen, M. G., Abbasi, R., Abdou, Y., et al. 2013b, *PhRvD*, **88**, 042004
 Aartsen, M. G., Abraham, K., Ackermann, M., et al. 2015a, *EPJC*, **75**, 492
 Aartsen, M. G., Abraham, K., Ackermann, M., et al. 2016, *ApJ*, **826**, 220
 Aartsen, M. G., Abraham, K., Ackermann, M., et al. 2017a, *ApJ*, **835**, 45
 Aartsen, M. G., Ackermann, M., Adams, J., et al. 2013c, *Sci*, **342**, 1242856
 Aartsen, M. G., Ackermann, M., Adams, J., et al. 2014, *PhRvL*, **113**, 101101
 Aartsen, M. G., Ackermann, M., Adams, J., et al. 2015b, *ApJ*, **809**, 98
 Aartsen, M. G., Ackermann, M., Adams, J., et al. 2015c, arXiv:1510.05223
 Aartsen, M. G., Ackermann, M., Adams, J., et al. 2017b, *JINST*, **12**, 03012
 Aartsen, M. G., Ackermann, M., Adams, J., et al. 2017c, *ApJ*, **839**, 67
 Aartsen, M. G., Ackermann, M., Adams, J., et al. 2018, *Sci*, **361**, 147
 Abbasi, R., Abdou, Y., Ackermann, M., et al. 2013, *NIMPA*, **700**, 188
 Abbasi, R., Ackermann, M., Adams, J., et al. 2009, *NIMPA*, **601**, 294
 Abdalla, H., Abramowski, A., Aharonian, F., et al. 2018, *A&A*, **612**, A1
 Abdo, A. A., Allen, B., Aune, T., et al. 2008, *ApJ*, **688**, 1078
 Abeysekara, A. U., Albert, A., Alfaro, R., et al. 2017, *ApJ*, **843**, 40
 Abramowski, A., Acero, F., Aharonian, F., et al. 2011a, *A&A*, **525**, A46
 Abramowski, A., Acero, F., Aharonian, F., et al. 2011b, *A&A*, **533**, A103
 Abramowski, A., Acero, F., Aharonian, F., et al. 2012, *A&A*, **541**, A5
 Abramowski, A., Aharonian, F., Benkhali, F. A., et al. 2016, *Natur*, **531**, 476
 Acero, F. 2011, *ICRC (Beijing)*, **32**, 185
 Acero, F., Ackermann, M., Ajello, M., et al. 2016, *ApJS*, **223**, 26
 Acero, F., Aharonian, F., Akhperjanian, A. G., et al. 2011, *A&A*, **525**, A45

- Acharya, B., Actis, M., Aghajani, T., et al. 2013, *A&A*, **43**, 3
- Ackermann, M., Ajello, M., Atwood, W. B., et al. 2012, *ApJ*, **750**, 3
- Aharonian, F., Akhperjanian, A. G., Aye, K.-M., et al. 2005, *A&A*, **435**, L17
- Aharonian, F., Akhperjanian, A. G., Aye, K.-M., et al. 2005, *A&A*, **442**, 1
- Aharonian, F., Akhperjanian, A. G., Bazer-Bachi, A. R., et al. 2006, *ApJ*, **636**, 777
- Aharonian, F., Akhperjanian, A. G., Bazer-Bachi, A. R., et al. 2006, *A&A*, **456**, 245
- Aharonian, F., Akhperjanian, A. G., de Almeida, U. B., et al. 2008, *A&A*, **477**, 353
- Ahlers, M., Bai, Y., Barger, V., & Lu, R. 2016, *PhRvD*, **93**, 013009
- Ahlers, M., & Murase, K. 2014, *PhRvD*, **90**, 023010
- Ahn, E.-J., Engel, R., Gaisser, T. K., et al. 2009, *PhRvD*, **80**, 094003
- Albert, A., André, M., Anghinolfi, M., et al. 2018, *ApJL*, **868**, L20
- Apel, W. D., Arteaga-Velázquez, J. C., Bekk, K., et al. 2017, *ApJ*, **848**, 1
- Balogopal, V. A., Haungs, A., Huege, T., & Schröder, F. G. 2018, *Eur. Phys. J.*, **C78**, 111
- Bartoli, B., Bernardini, P., Bi, X. J., et al. 2015, *ApJ*, **806**, 20
- Battistoni, G., Cerutti, F., Fassò, A., et al. 2007, in AIP Conf. Proc. 896, Hadronic Shower Simulation Workshop, ed. M. Albrow & R. Raja (Melville, NY: AIP), 31
- Benbow, W., Archambault, S., Archer, A., et al. 2017, in AIP Conf. Proc. 1792, 6th International Symposium on High Energy Gamma-Ray Astronomy, ed. F. A. Aharonian et al. (Melville, NY: AIP), 050001
- Borione, A., Catanese, M. A., Chantell, M. C., et al. 1998, *ApJ*, **493**, 175
- Braun, J., Dumm, J., Palma, F. D., et al. 2008, *A&A*, **489**, 299
- Carrigan, S., Brun, F., Chaves, R. C. G., et al. 2013, ICRC (Rio de Janeiro), **33**, 952
- Crawford, F., Gaensler, B. M., Kaspi, V. M., et al. 2001, *ApJ*, **554**, 152
- Cui, S., Liu, Y., Liu, Y., & Ma, X. 2014, *A&A*, **54**, 86
- Dame, T. M., Hartmann, D., & Thaddeus, P. 2001, *ApJ*, **547**, 792
- de los Reyes, R., Zajczyk, A., Chaves, R. C. G., et al. 2012, arXiv:1205.0719
- Djannati-Ataï, A., Marandon, V., Terrier, R., Chaves, R., et al. 2010, 38th COSPAR Scientific Assembly, 2811
- Drees, M., Halzen, F., & Hikasa, K. 1989, *PhRvD*, **39**, 1310
- Gaensler, B., Brazier, K., Manchester, R., Johnston, S., & Green, A. 1999, *MNRAS*, **305**, 724
- Gaggero, D., Grasso, D., Marinelli, A., et al. 2015a, *ApJL*, **815**, L25
- Gaggero, D., Urbano, A., Valli, M., & Ullio, P. 2015b, *PhRvD*, **91**, 083012
- Gaisser, T. K. 2006, *JPhCS*, **47**, 15
- Gorski, K. M., Hivon, E., Banday, A. J., et al. 2005, *ApJ*, **622**, 759
- Guo, X.-L., Xin, Y.-L., Liao, N.-H., et al. 2017, *ApJ*, **835**, 42
- Halzen, F., Kappes, A., & Murchadha, A. O. 2009, *PhRvD*, **80**, 083009
- Heck, D., Knapp, J., & Capdevielle, J. N. 1998, Forschungszentrum Karlsruhe Report FZKA 6019
- Hofverberg, P., Chaves, R. C. G., Fiasson, A., et al. 2010, in Proc. of Science, 25th Texas Symp. Relativistic Astrophysics, ed. F. M. Rieger, C. van Eldik, & W. Hofmann (Trieste: SISSA), 196, <http://pos.sissa.it/cgi-bin/reader/conf.cgi?confid=123>
- Huber, T., Kelley, J., Kunwar, S., Tosi, D., et al. 2017, *ICRC (Busan)*, **35**, 401
- Hunter, S. D., Bertsch, D. L., Catelli, J. R., et al. 1997, *ApJ*, **481**, 205
- Ingelman, G., & Thunman, M. 1996, arXiv:hep-ph/9604286
- Joshi, J. C., Winter, W., & Gupta, N. 2014, *MNRAS*, **439**, 3414
- Kachelriess, M., & Ostapchenko, S. 2014, *PhRvD*, **90**, 083002
- Kalberla, P. M., & Kerp, J. 2009, *A&A*, **47**, 27
- Keith, M., Johnston, S., Kramer, M., et al. 2008, *MNRAS*, **389**, 1881
- Kishishita, T., Bamba, A., Uchiyama, Y., Tanaka, Y., & Takahashi, T. 2012, *ApJ*, **750**, 162
- Lipari, P., & Vernetto, S. 2018, *PhRvD*, **98**, 043003
- Neyman, J. 1941, *Biometrika*, **32**, 128
- Ostapchenko, S. 2011, *PhRvD*, **83**, 014018
- Pedregosa, F., Varoquaux, G., Gramfort, A., et al. 2011, *J. Mach. Learn. Res.*, **12**, 2825
- Plum, M., Aartsen, M. G., Ackermann, M., et al. 2018, TeV Particle Astrophysics, <https://indico.desy.de/indico/event/18204/session/15/contribution/215>
- Protheroe, R. J., & Biermann, P. L. 1996, *A&A*, **6**, 45
- Rauw, G., Sana, H., & Nazé, Y. 2011, *A&A*, **535**, A40
- Rawlins, K., & Feusels, T. 2015, *ICRC (The Hague)*, **34**, 334
- Renaud, M., Goret, P., Chaves, R. C. G., et al. 2008, in AIP Conf. Ser. 1085, High Energy Gamma-Ray Astronomy, ed. F. A. Aharonian, W. Hofmann, & F. Rieger (Melville, NY: AIP), 281
- Risse, M., & Homola, P. 2007, *MPLA*, **22**, 749
- Romoli, C., Bordas, P., Mariaud, C., et al. 2017, *ICRC (Busan)*, **35**, 675
- Sun, M., ru Wang, Z., & Chen, Y. 1999, *ApJ*, **511**, 274
- Tluczykont, M., Hampf, D., Horns, D., et al. 2014, *A&A*, **56**, 42
- Van Overloop, A. 2011, *ICRC (Beijing)*, **32**, 97
- van Santen, J., Aarsten, M. G., Ackermann, M., et al. 2017, *ICRC (Busan)*, **35**, 991
- Vernetto, S., & Lipari, P. 2017, *ICRC (Busan)*, **35**, 718
- Wakely, S. P., & Horan, D. 2008, ICRC (Mérida), **30**, 1341
- Yang, R., Aharonian, F., & Evoli, C. 2016, *PhRvD*, **93**, 123007